Global carbon dioxide efflux from rivers enhanced by high nocturnal emissions

Lluis Gomez-Gener, Gerard Rocher-Ros, Tom Battin, Matthew J. Cohen, Higo J. Dalmagro, Kerry J. Dinsmore, Travis W. Drake, Clement Duvert, Alex Enrich Prast, Asa Horgby, Mark S. Johnson, Lily Kirk, Fausto Machado-Silva, Nicholas S. Marzolf, Mollie J. McDowell, William H. McDowell, Heli Miettinen, Anne K. Ojala, Hannes Peter, Jukka Pumpanen, Lishan Ran, Diego A. Riveros-Iregui, Isaac R. Santos, Johan Six, Emily H. Stanley, Marcus B. Wallin, Shane A. White and Ryan A. Sponseller

Enhanced nocturnal emissions of carbon dioxide amplify the role of streams in the global carbon cycle

Lluís Gómez-Gener[1, ♣,*], Gerard Rocher-Ros[2 ♣,*], Tom Battin[1], Matthew J. Cohen[3], Higo Dalmagro[4], Kerry J. Dinsmore[5], Travis Drake[6], Clément Duvert[7], Alex E. Prast[8], Åsa Horgby[1], Mark Johnson[9], Lily Kirk[10], Fausto Machado-Silva[11], Nicholas Marzolf[12], Mollie J. McDowell[9], William H. McDowell[13], Heli Miettinen[14], Anne K. Ojala[14], Hannes Peter[1], Jukka Pumpanen[15], Diego Riveros-Iregui[16], Isaac Santos[17], Johan Six[6], Emily H. Stanley[17], Marcus B. Wallin[18], Shane White[19], Ryan A. Sponseller[2]

[1] Stream Biofilm and Ecosystem Research Laboratory, School of Architecture, Civil and Environmental Engineering, Ecole Polytechnique Fédérale de Lausanne, Lausanne, Switzerland

[2] Department of Ecology and Environmental Science, Umeå University, Umeå, Sweden

[3] School of Forest Resources and Conservation, University of Florida, USA

[4]

[5] Centre for Ecology and Hydrology, Bush Estate, Penicuik, UK.

[6]

[7] Research Institute for the Environment and Livelihoods, Charles Darwin University, Darwin, Australia

[8]

[9] Institute for Resources, Environment and Sustainability and Department of Earth, Ocean and Atmospheric Sciences, University of British Columbia, Vancouver, Canada

[10] School of Natural Resources and Environment, University of Florida, USA

[11]

[12] Department of Forestry and Environmental Resources, North Carolina State University, Raleigh, NC, USA

[13] Department of Natural Resources and the Environment, University of New Hampshire, Durham, NH USA

[14] University of Helsinki, Faculty of Biological and Environmental Sciences, Ecosystems and Environment Research Programme, Helsinki, Finland

[15] University of Eastern Finland, Department of Environmental and Biological Sciences, Kuopio, Finland

[16]

[17] Center for Limnology and Department of Integrative Biology, University of Wisconsin-Madison

[18] Department of Aquatic Sciences and Assessment, Swedish University of Agricultural Sciences, Uppsala, Sweden

[19]

♣ Authors contributed equally to the development of the manuscript.

* Corresponding authors: Lluís Gómez-Gener (luis.gomezgener@epfl.ch) Gerard Rocher-Ros (gerard.rocher@umu.se)

Abstract

Carbon dioxide (CO_2) emissions to the atmosphere from running waters are estimated to be four times larger than the total carbon (C) flux to the oceans. However, these fluxes remain poorly constrained because of substantial temporal variability in dissolved CO_2 concentrations. Using a global compilation of high frequency CO_2 measurements, we demonstrate that nocturnal CO_2 emissions are consistently larger, by an average of 27% (0.9 g C m^{-2} d^{-1}), than those estimated from diurnal concentrations alone. Canopy shading is the principal control on observed diel (24 hr) variation, suggesting this nocturnal increase arises from daytime fixation of dissolved inorganic C by photosynthesis. Because contemporary global estimates of CO_2 emissions to the atmosphere from running waters (0.65 – 1.8 Pg C yr^{-1}) rely primarily on discrete measurements of dissolved CO_2 obtained during the day, they substantially underpredict the magnitude of this important flux. Accounting for night-time CO_2 elevates global estimates of emissions from running waters to the atmosphere by 0.20-0.55 Pg C yr^{-1}.

Carbon dioxide (CO_2) emission from inland waters to the atmosphere is a major flux in the global carbon (C) cycle, and four-fold larger than the lateral C export to oceans[1]. Streams and rivers are hotspots for this flux, accounting for ~85% of inland water CO_2 emissions despite covering <20% of the freshwater surface area[2]. Despite this importance, the magnitude of global CO_2 emissions from streams and rivers remains highly uncertain with estimates revised upwards over the past decade from 0.6 to 3.48 Pg C yr^{-1} [(3,4)]. Changes to this estimate follow improvements in the spatial resolution for upscaling emissions[2,5], as well as new studies from previously underrepresented areas such as the Congo[6], Amazon[7], and global mountains[8]. Further refinements have emerged from considering temporal variability in CO_2 emission rates[9]. However, despite recent studies showing dramatic day-night changes in stream and river water CO_2 concentrations[10–14] the significance of systematic sub-daily variation on overall CO_2 emissions remains unexplored.

Diurnal cycles in solar radiation impose a well-known periodicity on stream biogeochemical processes, creating diel (i.e., 24-hr period lengths) patterns for many solutes and gases, including nutrients, dissolved organic matter, and dissolved oxygen (O_2)[15]. Indeed, diel variation in O_2 arising from photosynthetic activity is the signal from which whole-system metabolic fluxes are estimated[16]. Photosynthetic production of O_2 is stoichiometrically linked to the day-time assimilation of dissolved inorganic carbon (principally bicarbonate and dissolved CO_2), lowering CO_2 concentrations during the day. The resulting diel variation, with higher night-time CO_2 concentrations when respiration reactions dominate, implies increased emissions at night. Despite the obvious connection between photosynthesis and CO_2 consumption, the implications for total aquatic CO_2 emissions has been neglected, most likely due to the lack of sub-daily measurements of CO_2 in water[17]. Notably, other processes can also vary at sub-daily time scales and could thus similarly drive diel change in CO_2 emissions from streams, including interactions with the carbonate system[18], photo-chemical oxidation of organic matter[19], and diel changes in discharge and subsequently lateral CO_2 inputs from terrestrial environments[20]. Regardless, the overall magnitude and direction of diel changes in CO_2 concentrations and the associated consequences for emissions are largely unknown.

Current global estimates of CO_2 emissions from running waters rely almost exclusively on manually collected samples that fail to incorporate sub-daily variability. Here, we assess whether reliance on these samples creates a strong temporal sampling bias by using the most widely used global river chemistry database (GLORICH[21]). Next, we leverage recent technological advances in continuous, sensor-based dissolved CO_2 monitoring[17] to ask if this sampling bias is concurrent with consistent day-night differences in CO_2 emission rates from streams. To do this, we compiled high-resolution CO_2 time series representing a total of 52 years of continuous data (Table S1) from 66 streams that span a wide range of climate, land cover, and stream physicochemical properties (Table S2). We evaluated the generality of diurnal stream CO_2 variation, quantified the significance of these signals for CO_2 emissions, and identified the main landscape factors that control diurnal variation. Finally, we estimated the potential bias in global CO_2 stream emission estimates that arise from neglecting nocturnal emissions.

Results and Discussion

Magnitude and bias of diel changes in CO_2 emissions

Water samples compiled in the GLORICH database[21] are primarily taken during the day, with 90% of samples collected between 08:10 and 15:55 and a median sampling hour of 11:25 (Figure 1a). Comparing this time window of manual sampling with sensor data synthesized in this study, we found that only 10% of days had maximum CO_2 emissions within these hours, and there was a consistent pattern of higher emission rates during night than day (Figure 1b).

On average, nocturnal emission rates were 27.2% greater than daytime rates across all sites, with differences ranging from −11.8 to 192.5 % (Table S3). While this overall pattern was geographically consistent, with 56 of 66 (85%) of sites showing higher average nocturnal CO_2 emission rates (Figure 2a and Table S3), the observed ranges in diel change varied among biomes (Figure 2b). Specifically, streams with the largest diel change in emissions drained temperate forests, followed by montane grasslands; however, these biomes also had the largest internal variation. By comparison, we observed generally smaller diel changes, and less internal variability, for boreal and tropical/sub-tropical systems. Despite such differences, the large variation observed within most biomes suggests that controls over these patterns operate at finer spatial scales[13]. Further, because the GLORICH database – the foundation of current global estimates of CO_2 emissions from inland waters[2] – relies primarily on manual samples with a strong daytime sampling bias, the geographically widespread diel variation in CO_2 emissions introduces a systematic and potentially large error in estimates of aggregate flux rates.

Drivers of diel changes in CO_2 emissions

Diel patterns in stream CO_2 emissions are the result of a dynamic interplay between biogeochemical and hydrological processes that adjust stream CO_2 concentrations at the daily scale – theses include aquatic primary production[11,13], biological[22] and photolytic oxidation of organic C[19], and terrestrial import of CO_2 from soil respiration and mineral weathering[20]. Additionally, diel changes in water temperature can affect CO_2 emissions through its effect on the physical exchange rate between air and water (kCO_2)[23] . An initial exploration of our continuous data suggest that aquatic processes generate considerable temporal variation in the magnitude of diel variation in emissions (Figure 3). Specifically, the largest diel amplitudes were consistently observed during summer, and in open canopy reaches (median = 0.76 g C m^{-2} d^{-1}). Markedly reduced amplitudes were observed in streams with closed canopies (median = 0.09 g C m^{-2} d^{-1}), while intermediate amplitudes were evident at partially covered sites (median=0.37 g C m^{-2} d^{-1}). Overall, these observations are consistent with greater levels of daytime CO_2 uptake in open canopy streams during summer, when warm temperatures and greater incident light [24,25] support elevated rates of photosynthesis[11]. By contrast, wintertime diel changes in stream CO_2 emissions are more similar across canopy cover categories, suggesting reduced aquatic photosynthesis.

We used structural equation modeling (SEM) to further resolve factors and causal combinations that underpin variation in summertime diel emissions, the time-period for which have the most complete data set (Table S1). Our structural model consisted of two levels of factor interaction, or metamodels (see method section for a more detailed description of the SEM). First, we considered whether diel CO_2 emission patterns arise from parallel variation in kCO_2 and stream water pCO_2, the two main factors determining aquatic CO_2 emissions[26]. The results from the SEM for at this first level (r^2=0.43; Figure S4 and Table S4) suggest that diel variation in CO_2 emissions was mostly driven by variation in pCO_2 (β=0.65), whereas kCO_2 exerted a minor influence (β=0.02). Second, we used SEM to identify significant relationships between a set of environmental variables and the diel changes in pCO_2. This second SEM model (r^2=0.46; Figure 3 and Table S4) indicated that stream canopy cover (β=−0.58) was the primary driver of diel variation of pCO_2, with channel slope (β=−0.18), stream NO_3^- concentration (β=0.25) and diel temperature variation (β=0.13) as secondary drivers. Together with the observed seasonal patterns (Figure 3), SEM results support the hypothesis that riparian canopy cover drives diel pCO_2 variation by regulating the light reaching the stream surface and, in turn, daytime rates of stream autotrophic CO_2 uptake during[16,27,28].

Diel patterns in CO_2 emissions in running waters not only varied seasonally but also spatially, increasing with drainage size (Figure 4a). In larger river systems, terrestrial shading of the channel is reduced, increasing the light available for primary producers[24], which ultimately explains the general increase in GPP with channel size[29,30]. Still, we observed larger rivers with open canopies that do not sustain significant diel change in CO_2 evasion (Figure 4b). This dampening of diel amplitude likely results from light-attenuation in the water column, for example linked to high concentrations of dissolved organic matter (DOM) that inhibit GPP[31] (Figure 4c; Figure S6). Thus, light attenuation, whether caused by canopy cover along small streams, or by water colour, turbidity, or depth for larger river systems[32], dictates the overall magnitude of diel changes in CO_2 emissions along river continua. We explored the potential influences of water colour more deeply at the sub-tropical Florida sites, where we have continuous CO_2 and fDOM in five rivers spanning a large range in DOC (0.96-43.4 ppm) and ecosystem size (9.0-66.7 median daily discharge). High frequency data from these sites confirm that diel changes in CO_2 emissions are supressed above ca.70 ppb of fDOM (corresponding to ca. 20 mg L^{-1} DOC), despite relatively high incident light (Figure 4d). Overall, given that aquatic photosynthesis tends to increase with drainage size, because lowland systems are less shaded and more often subject to nutrient enrichment via human activities[30], it is reasonable to predict that the importance of diel variation in CO_2 emissions found in this study for smaller systems would persist for large rivers, as long as light attenuation in the water column permits.

The controls on potential diel change in CO_2 emissions exerted by either canopy cover or water color are highly variable in space, and do not follow strict geographical patterns (Fig. 2). Yet, the probability that one or both of these constraints operates is likely biome-specific and this may aid in understanding which regions of Earth are more prone to strong bias in upscaling. For example, boreal and tropical regions are typically characterized by forests with dense canopies and can support aquatic systems with dark, DOC-rich waters (refs; Fig S3). Indeed, for these biomes we observed, on average, a lower diel change in CO_2 emissions (Fig. 2b). In this context, observations from the sub-tropical Florida sites likely provide insight into the dynamics that would be expected for dark water systems elsewhere, particularly tropical rivers, which are otherwise poorly represented in our analysis. For some biomes (e.g., montane grasslands and tundra), vegetation structure and edaphic properties make light constraints on aquatic GPP and diel CO_2 evasion less likely, while in other settings (e.g., the temperate zone) the influences of land cover change and/or anthropogenic nutrient enrichment may play particularly important roles[30]. Overall, we suggest that future efforts to the resolve the fine-scale spatial patterns of canopy cover and DOM in flowing waters could be used for a more refined understanding of aquatic GPP and its implications for CO_2 emissions.

Implications for global CO_2 emissions from stream networks

Our analysis reveals three facts with important consequences for global estimates of CO_2 emissions from running waters: (1) current estimates based on manual samples are heavily biased towards day-time, (2) CO_2 emission rates are consistently higher at night-time due to variations in aquatic pCO_2, and (3) this pattern is primarily driven by light availability and is widespread across biomes and along river continua. To further quantify this underestimation of CO_2 emissions we compare the measured total emissions for each site with the emissions estimated considering only the CO_2 concentrations observed between 10:00 and 14:00 (the interquartile sampling time in the GLORICH database (Figure 1a). Across all sites, CO_2 emissions integrated over a full day were 34.7% higher than those based on samples taken at midday (range: −6.6 – 369 %; bootstrapped 95% confidence interval: 14.0 – 46.7 %). Based on the two current global estimates of stream CO_2 emissions of 0.6-1.8 Pg C yr^{-1} [(2,33)], this proportional bias results in an additional 0.20 – 0.55 Pg C yr^{-1} of CO_2 evaded from streams globally (bootstrapped 95% confidence interval: 0.09 – 0.30; 0.25 – 0.84, respectively). However, given that the current global estimates of C emissions from running waters are still highly uncertain and conflict global C budgets[34] this additional flux of CO_2 should be taken with caution until future global estimates are refined.

We also emphasize that there are other important sources of uncertainty embedded in the global estimates of emissions from streams, upon which our estimate is based. For example, current estimates[4,33] are still derived from indirect determinations of surface water CO_2 from alkalinity and pH, which can be highly uncertain[35,36]. Further, the notoriously variable nature of hydrodynamic factors that influence CO_2 emissions cannot easily be aggregated at large spatial scales[11,37]. It is also problematic that current estimates remain biased towards observations from mid-to-high latitudes, while unrepresented areas such as the Tropics are thought to be key contributors to the global CO_2 emissions from streams[6,38]. Our study, despite covering most biomes and spanning large gradients in canopy cover and water colour, also suffers from this bias. Despite this, our assessment represents the first compilation of direct, high-temporal resolution measurements of CO_2 in flowing waters from across the globe, which will be a key piece in refining global estimates of CO_2 emissions from inland waters. While the magnitude of this global estimate can be further refined, the broad consistency and strength of the patterns observed here suggest that nocturnal emissions of CO_2 from streams and rivers is a major unaccounted flux in the global C cycle.

Methods

Study sites and data acquisition

We compiled high-frequency dissolved CO_2 time-series (median temporal resolution = 39 min; range 5 to 180 min) over at least eight days (median time series duration = 317 days; range 8 to 1553 days) from 66 headwater streams worldwide (Figure 2a; Table S1). We used median annual discharge (which covaried with catchment surface area; Figure S5) as a criterion to select streams (i.e., median annual discharge < 1.5 m^3 s^{-1}, catchment area < 246 km^2; orders 1 to 3[39]). Selected streams span biomes, including tropical forests and savanna, temperate forests, boreal forest and taiga, arctic tundra, high-mountain forests and grasslands and, accordingly, a wide range of climatic and biogeographic conditions (Table S2). They also encompass a variety of catchment features (e.g., land cover, altitude, and surface area) and reach-scale hydrological, morphometric, and physicochemical properties (Table S2).

High-frequency CO_2 measurements were obtained from a variety of sources, including unpublished time-series, monitoring network platforms (e.g., StreamPulse, https://data.streampulse.org/), and literature datasets (Table S2). In all the cases, CO_2 was measured using *in-situ* automated sensors connected to data loggers (Table S2). The measurement accuracy of the CO_2 sensors ranged from ±1% to ±3%. In addition, water temperature (in all streams) and discharge (in 57 of 66 streams) were also measured at the same frequency as CO_2 using *in-situ* automated sensors.

Time-series processing

We standardized each time-series to an hourly time step by resampling higher frequency measurements and interpolating lower frequency measurements. We also normalized CO_2 concentrations to CO_2 partial pressures ($p$$CO_2$, ppm), corrected for temperature and pressure variation, and removed obvious measurement errors ($p$$CO_2 < 0$ ppm). Continuous discharge was calculated from stage-discharge rating curves developed from existing discharge measurements. In total, the high-frequency dataset used for analysis included 457,637 hourly CO_2, temperature and discharge observations. 32 time series covered at least one complete year, 7 covered more than 200 days while the remaining 27 covered between 8 and 198 days, mostly during the summer (Figure S1).

Compilation of ancillary variables

Stream reach canopy cover was determined by visually inspecting orthophotos of the study sites. High-resolution orthophotos from Google Earth imagery were downloaded at the highest resolution possible using the "ggmap" package in R (version 3.0.0), and classified in three categories of "no cover" (0), "partly covered" (1), or "fully covered" (2). The "no cover" category was selected when it was possible to see the full extent of the stream channel, "partly covered" when some parts of the stream were visible, and "fully covered" when it was not possible to detect the presence of a stream based on an orthophoto (Figure S3).

Stream channel slope was determined by measuring the difference in elevation between the sampling location and 300 meters upstream following the channel. To do this, we downloaded digital elevation models (DEM) at resolutions ranging between 1.9 – 14 m (depending on the location) using the "elevatr" package in R (version 0.2.0). Then, for each site a raster of the flow-accumulation was produced using the "whitebox" package in R (version 0.5.0), after initially breaching depressions for hydrological correctness. By combining the flow-accumulation raster with the DEM, we extracted the stream path and the elevation at the site and 300 m upstream (in ArcGIS 10.5).

Land cover was determined using the Global Land Cover Maps (100m resolution; Copernicus Global Land Service) and the catchment boundaries delineated using a high resolution DEMs (2x2m) in QGIS 3.2.1. Mean annual concentrations (not flow-weighted) of dissolved organic carbon (DOC), nitrate (NO_3^-), ammonium (NH_4^+), pH and conductivity for the study streams were obtained from unpublished sources or extracted from the literature. Mean annual stream discharge, as well as water temperature, were computed from hourly time series.

Determination of CO_2 emissions

We estimated CO_2 emissions as the product of the gas transfer velocity (k_{CO2}) and the concentration of dissolved CO_2 relative to atmospheric equilibrium[26]. A standardized gas transfer velocity (k_{600}) was obtained based on the stream energy dissipation (eD)[40], defined as the product of channel slope (S; m m^{-1}), water velocity (V; m s^{-1}) and acceleration due to gravity (g; 9.8 m s^{-2}). We then calculated k_{600} as $k_{600} = e^{(3.1 + 0.35\times\log(eD))}$ for eD < 0.02 m^{-2} s^{-3}; and as $k_{600} = e^{(6.43 + 1.18\times\log(eD))}$ for eD > 0.02 m^{-2} s^{-3}. Water velocity was modelled using a power-law relationship with discharge[26]; in 4 streams discharge data were not available and we used a constant velocity of 0.2 m s^{-1}. The k_{600} was converted to a gas- and temperature-specific gas transfer velocity k_{CO2}, using the temperature-dependent Schmidt numbers for CO_2 [26]. Potential day-night differences in gas exchange required separate night and day k_{CO2} calculations with time-of-day specific velocity and temperature values. The CO_2 disequilibrium relative to the atmosphere was calculated as the difference in water and air pCO_2, converted to molar CO_2 concentrations using the temperature-specific Henry's constant. Atmospheric pCO_2 was assigned monthly to each site from the global average measured by the Global Monitoring Laboratory of NOAA (https://www.esrl.noaa.gov/gmd/ccgg/trends/global.html), which contains measurements between 2007 to 2020, which align with our study. We assessed the importance of sub-daily changes in atmospheric concentrations by examining atmospheric measurements of pCO_2 from 14 streams and 77 ecosystem flux towers of globally. We concluded that day-night changes in atmospheric pCO_2 are small and inconsistent, and therefore poorly constrained for extrapolation to other stream sites (See Supplementary Text 1).

Finally, to assess whether a day-time sampling bias exists, we determined the distribution of sampling time in the GLORICH database[21]. From the database, we filtered all sampling occasions where both CO_2 (calculated from alkalinity and pH) and the time of sampling were available (n = 733,977, from 8,520 locations), we then extracted summary statistics such as the median, 90% range and the interquartile range to compare with sensor measurements.

Statistical analyses

We examined a variety of metrics to characterize sub-daily and between-day variation. To quantify the underestimation in CO_2 emissions due to a day-time bias, we compared total CO_2 emissions estimated using hourly measurements with total emissions estimated from the average measurements between 10:00 and 14:00, the interquartile range of the observations in the GLORICH database. Given the non-normality of results among sites, we present uncertainty as normal bootstrapped intervals using the "boot" package in R (version 1.3-24), with 10,000 replications. We quantified median CO_2 emissions (g C m^{-2} d^{-1}) during the day (between 12:00 and 17:00), median CO_2 emissions during the night (between 00:00 and 05:00), the absolute difference between day and night CO_2 emissions, and the relative difference in CO_2 concentrations between day and night (in %; $((CO_{2,\,NIGHT} - CO_{2,\,DAY}) / CO_{2,\,DAY}) \times 100$). Also, to evaluate differences between canopy levels we used the non-parametric Kruskal–Wallis test.

We explored temporal patterns of day-night CO_2 emissions differences to test the influence of seasonality, local canopy cover, and their interaction. We used piecewise structural equation modelling (SEM) to evaluate causal and directional links between physical and biological parameters operating at the reach-scale (Table S2) and variance in daily day-night differences in CO_2 emissions. SEM is a theory-oriented multivariate statistical approach capable of testing a network of causal hypotheses by allowing evaluation of simultaneous influences rather than individual (bivariate) causes[41]. We first devised a metamodel (or metamodels) based on *a priori* theoretical knowledge and known mechanisms (see above and Figure 3). The metamodel was fitted and tested using the function psem() in the *piecewiseSEM* R Package (version 2.1). To evaluate the effect sizes of each interaction within metamodels, the psem() model output provides estimates of individual (standardized) path coefficients (β). The evaluation of goodness of fit and associated uncertainty is performed through the coefficient of determination (r^2) and the residual standard error (RSE), respectively. Compared with traditional variance-covariance based SEM, piecewise SEM allows for fitting of models to different distributions through a generalized linear model (GLM). SEM modelling was conducted using summer data only, which is when most of the sites are represented (see Figure S1).

Data availability

Data will be available at the open data repository Zenodo and can already be explored interactively at: https://gmrocher.shinyapps.io/night_co2_emissions_streams/.

References

1. Cole, J. J. *et al.* Plumbing the global carbon cycle: Integrating inland waters into the terrestrial carbon budget. *Ecosystems* **10**, 171–184 (2007).
2. Raymond, P. A. *et al.* Global carbon dioxide emissions from inland waters. *Nature* **503**, 355–9 (2013).
3. Drake, T. W., Raymond, P. A. & Spencer, R. G. M. Terrestrial carbon inputs to inland waters: A current synthesis of estimates and uncertainty. *Limnology and Oceanography Letters* (2017) doi:10.1002/lol2.10055.
4. Raymond, P. A. *et al.* Global carbon dioxide emissions from inland waters. *Nature* **503**, 355–359 (2013).
5. Lauerwald, R., Laruelle, G. G., Hartmann, J., Ciais, P. & Regnier, P. A. G. Spatial patterns in CO2 evasion from the global river network. *Global Biogeochemical Cycles* **29**, 534–554 (2015).
6. Borges, A. V. *et al.* Globally significant greenhouse-gas emissions from African inland waters. *Nature Geoscience* **8**, 637–642 (2015).
7. Sawakuchi, H. O. *et al.* Carbon Dioxide Emissions along the Lower Amazon River. *Frontiers in Marine Science* **4**, 1–12 (2017).
8. Horgby, Å. *et al.* Unexpected large evasion fluxes of carbon dioxide from turbulent streams draining the world's mountains. *Nature Communications* **10**, (2019).
9. Liu, S. & Raymond, P. A. Hydrologic controls on pCO 2 and CO 2 efflux in US streams and rivers . *Limnology and Oceanography Letters* **3**, 428–435 (2018).
10. Peter, H. *et al.* Scales and drivers of temporal pCO2 dynamics in an Alpine stream. *Journal of Geophysical Research: Biogeosciences* **119**, 1078–1091 (2014).

11. Rocher-Ros, G., Sponseller, R. A., Bergstr, A., Myrstener, M. & Giesler, R. Stream metabolism controls diel patterns and evasion of CO2 in Arctic streams. *Global Change Biology* 0–3 (2019) doi:10.1111/gcb.14895.

12. Wallin, M. B., Audet, J., Peacock, M., Sahlée, E. & Winterdahl, M. Carbon dioxide dynamics in an agricultural headwater stream driven by hydrology and primary production. 1–28 (2020).

13. Crawford, J. T., Stanley, E. H., Dornblaser, M. M. & Striegl, R. G. CO2 time series patterns in contrasting headwater streams of North America. *Aquat Sci* **79**, 473–486 (2017).

14. Reiman, J. & Xu, Y. J. Diel Variability of pCO2 and CO2 Outgassing from the Lower Mississippi River: Implications for Riverine CO2 Outgassing Estimation. *Water* **11**, 43 (2018).

15. Hensley, R. T. & Cohen, M. J. On the emergence of diel solute signals in flowing waters. *Water Resour. Res.* **52**, 759–772 (2016).

16. Odum, HT. Primary Production in Flowing Waters. *Limnol. Oceanogr* **1**, 102–117 (1955).

17. Johnson, M. S. *et al.* Direct and continuous measurement of dissolved carbon dioxide in freshwater aquatic systems-method and applications. *Ecohydrol.* **3**, 68–78 (2010).

18. Stets, E. G. *et al.* Carbonate buffering and metabolic controls on carbon dioxide in rivers. *Global Biogeochemical Cycles* **31**, 663–677 (2017).

19. Cory, R. M., Ward, C. P., Crump, B. C. & Kling, G. W. Sunlight controls water column processing of carbon in arctic fresh waters. *Science* **345**, 925–928 (2014).

20. Riml, J., Campeau, A., Bishop, K. & Wallin, M. B. Spectral decomposition reveals new perspectives on CO 2 concentration patterns and soil-stream linkages. 0–3 (2019) doi:10.1029/2018JG004981.

21. Hartmann, J., Lauerwald, R. & Moosdorf, N. A Brief Overview of the GLObal RIver Chemistry Database, GLORICH. *Procedia Earth and Planetary Science* **10**, 23–27 (2014).

22. Hotchkiss, E. R. *et al.* Sources of and processes controlling CO2 emissions change with the size of streams and rivers. *Nature Geosci* **8**, 696–699 (2015).

23. Demars, B. O. L. & Manson, J. R. Temperature dependence of stream aeration coefficients and the effect of water turbulence: A critical review. *Water Research* **47**, 1–15 (2013).

24. Koenig, L. E. *et al.* Emergent productivity regimes of river networks. *Limnol Oceanogr* **4**, 173–181 (2019).

25. Bernhardt, E. S. *et al.* The metabolic regimes of flowing waters: Metabolic regimes. *Limnol. Oceanogr.* **63**, S99–S118 (2018).

26. Raymond, P. A. *et al.* Scaling the gas transfer velocity and hydraulic geometry in streams and small rivers. *Limnology & Oceanography: Fluids & Environments* **2**, 41–53 (2012).

27. Mulholland, P. J. *et al.* Inter-biome comparison of factors controlling stream metabolism. *Freshwater Biology* **46**, 1503–1517 (2001).

28. Roberts, B. J., Mulholland, P. J. & Hill, W. R. Multiple scales of temporal variability in ecosystem metabolism rates: Results from 2 years of continuous monitoring in a forested headwater stream. *Ecosystems* **10**, 588–606 (2007).

29. Vanote, R. L., Minshall, W. G., Cummins, K. W., Sedell, J. R. & Cushing, C. E. The River Continuum Concept. *Canadian Journal of Fisheries and Aquatic Sciences* **37**, 130–137 (1980).

30. Finlay, J. C. Stream size and human influences on ecosystem production in river networks. *Ecosphere* **2**, art87 (2011).

31. Kirk, L., Hensley, R. T., Savoy, P., Heffernan, J. B. & Cohen, M. J. Estimating Benthic Light Regimes Improves Predictions of Primary Production and constrains Light-Use Efficiency in Streams and Rivers. *Ecosystems* (2020) doi:10.1007/s10021-020-00552-1.

32. Julian, J. P., Doyle, M. W., Powers, S. M., Stanley, E. H. & Riggsbee, J. A. Optical water quality in rivers. *Water Resour. Res.* **44**, (2008).

33. Lauerwald, R., Laruelle, G. G., Hartmann, J., Ciais, P. & Regnier, P. A. G. Spatial patterns in CO_2 evasion from the global river network: SPATIAL PATTERNS OF RIVERINE *P* CO_2 AND *F* CO_2. *Global Biogeochem. Cycles* **29**, 534–554 (2015).

34. Friedlingstein, P. *et al.* Global Carbon Budget 2019. *Earth Syst. Sci. Data* **11**, 1783–1838 (2019).

35. Liu, S., Butman, D. E. & Raymond, P. A. Evaluating CO_2 calculation error from organic alkalinity and pH measurement error in low ionic strength freshwaters. *Limnol Oceanogr Methods* **18**, 606–622 (2020).

36. Abril, G. *et al.* Technical Note: Large overestimation of <i>p</i>CO₂ calculated from pH and alkalinity in acidic, organic-rich freshwaters. *Biogeosciences* **12**, 67–78 (2015).

37. Duvert, C., Butman, D. E., Marx, A., Ribolzi, O. & Hutley, L. B. CO2 evasion along streams driven by groundwater inputs and geomorphic controls. *Nature Geosci* **11**, 813–818 (2018).

38. Richey, J. E., Melack, J. M., Aufdenkampe, A. K., Ballester, V. M. & Hess, L. L. Outgassing from Amazonian rivers and wetlands as a large tropical source of atmospheric CO2. *Nature* **416**, 617–620 (2002).

39. Guth, P. L. Drainage basin morphometry: a global snapshot from the shuttle radar topography mission. *Hydrol. Earth Syst. Sci.* **15**, 2091–2099 (2011).

40. Ulseth, A. J. *et al.* Distinct air–water gas exchange regimes in low- and high-energy streams. *Nat. Geosci.* **12**, 259–263 (2019).

41. Lapierre, J.-F., Guillemette, F., Berggren, M. & del Giorgio, P. a. Increases in terrestrially derived carbon stimulate organic carbon processing and CO2 emissions in boreal aquatic ecosystems. *Nature communications* **4**, 2972 (2013).

Acknowledgements

The authors thank John Crawford and Sam Blackburn for providing data in this study. The authors also thank Jens Hartmann for providing access to the GLORICH database. This study was supported by a FORMAS grant to R.A.S.

Author contributions:

L.G-G, G.R-R, and R.A.S designed the study and wrote the paper with inputs from M.J.C. L.G-G and G.R-R compiled, processed, and analyzed the data. Å.H. provided remote sensing estimates. All authors contributed with data and commented on the earlier versions of this manuscript.

Competing interests:

The authors declare no competing interests

Materials and Correspondence:

Lluís Gomez-Gener (luis.gomezgener@epfl.ch) and Gerard Rocher-Ros (gerard.rocher@umu.se)

Supplementary materials of:

Enhanced nocturnal emissions of carbon dioxide amplify the role of streams in the global carbon cycle

Supplementary text

ST1: Exploration of diel variation in atmospheric pCO_2

There is evidence of daily fluctuations in atmospheric pCO_2 near the surface in terrestrial ecosystems[1] which can therefore impact the estimates of CO_2 evasion. Here we assumed constant atmospheric pCO_2 given the lack of available data for the majority of sites. However, in a subset of sites (n=14) we have measured atmospheric pCO_2 above the stream surface. The median amplitude of the atmospheric pCO_2 for these streams is 7.8 ppm, with air pCO_2 increasing from day to night.

To further assess the consistency of this pattern we also explored the diel change in atmospheric pCO_2 measured by a network of eddy covariance towers worldwide (FLUXNET[2]). We compiled data from 77 sites that spanned a gradient in land cover and in the same geographical region as the stream sites (Figure S7). The median amplitude of air pCO_2 for different land cover types varied between 0 and 15 ppm, with a median for all sites of 4.2 ppm.

We have not corrected the atmospheric pCO_2 for diel changes for multiple reasons: (1) both for stream and terrestrial measurements there is substantial variability among sites, indicating that the drivers of this diel variability in atmospheric pCO_2 are hard to constrain and therefore extrapolate to other sites; (2) the diel amplitudes in atmospheric pCO_2 are more than one order of magnitude lower than aquatic counterparts (median of all sites: 102 ppm, range: 0 – 1515 ppm); (3) and the atmospheric diel changes are close to the accuracy of the sensors (see Table S1 for accuracy of different sensors). We acknowledge that diel changes in atmospheric pCO_2 can be important in specific sites and/or dates due to topographic depressions, closed canopy, or micrometeorological conditions, but without further data is not possible to confidently correct for this process.

Supplementary Figures

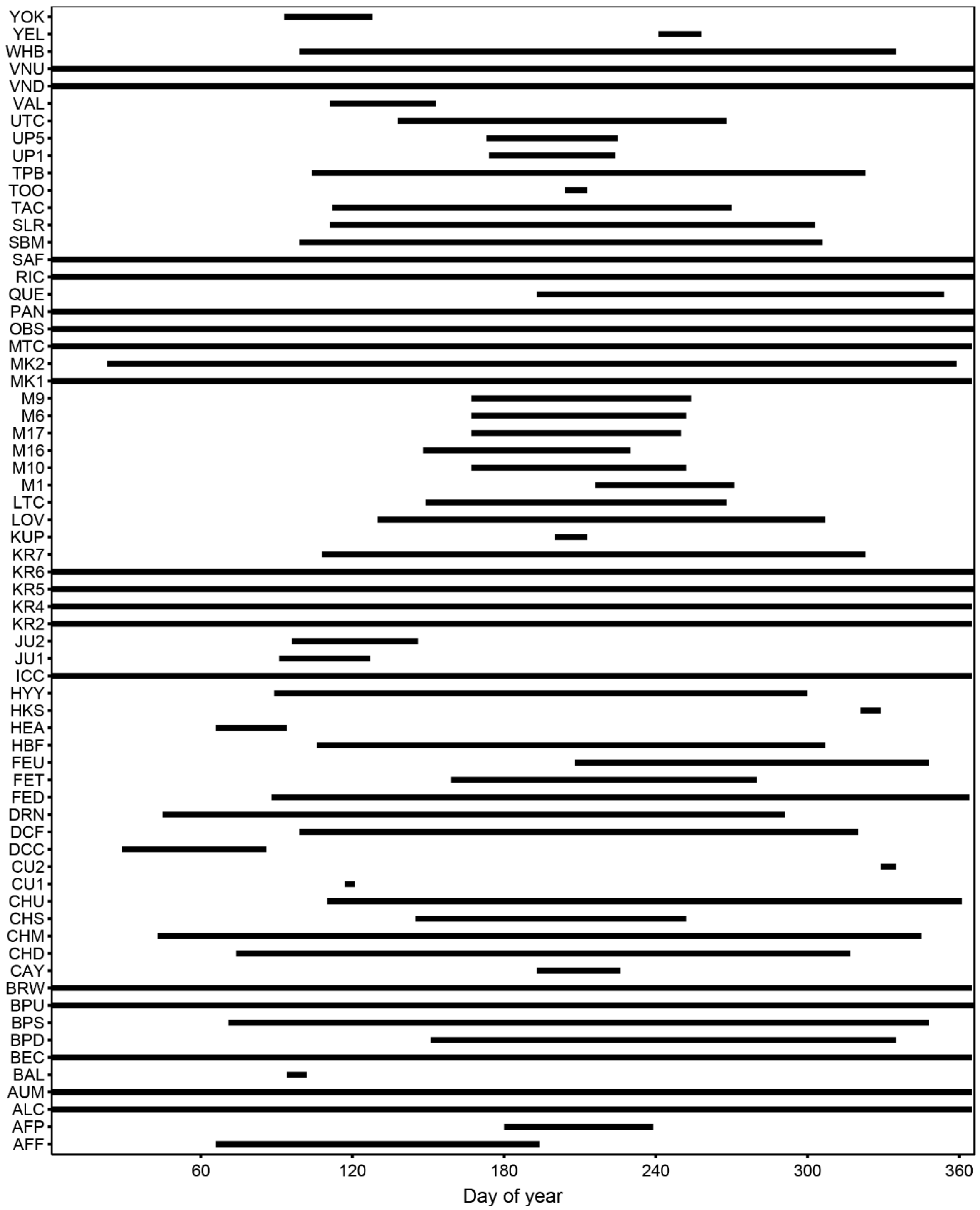

Figure S1. Intra-annual coverage of the high-frequency dataset used for the analysis.

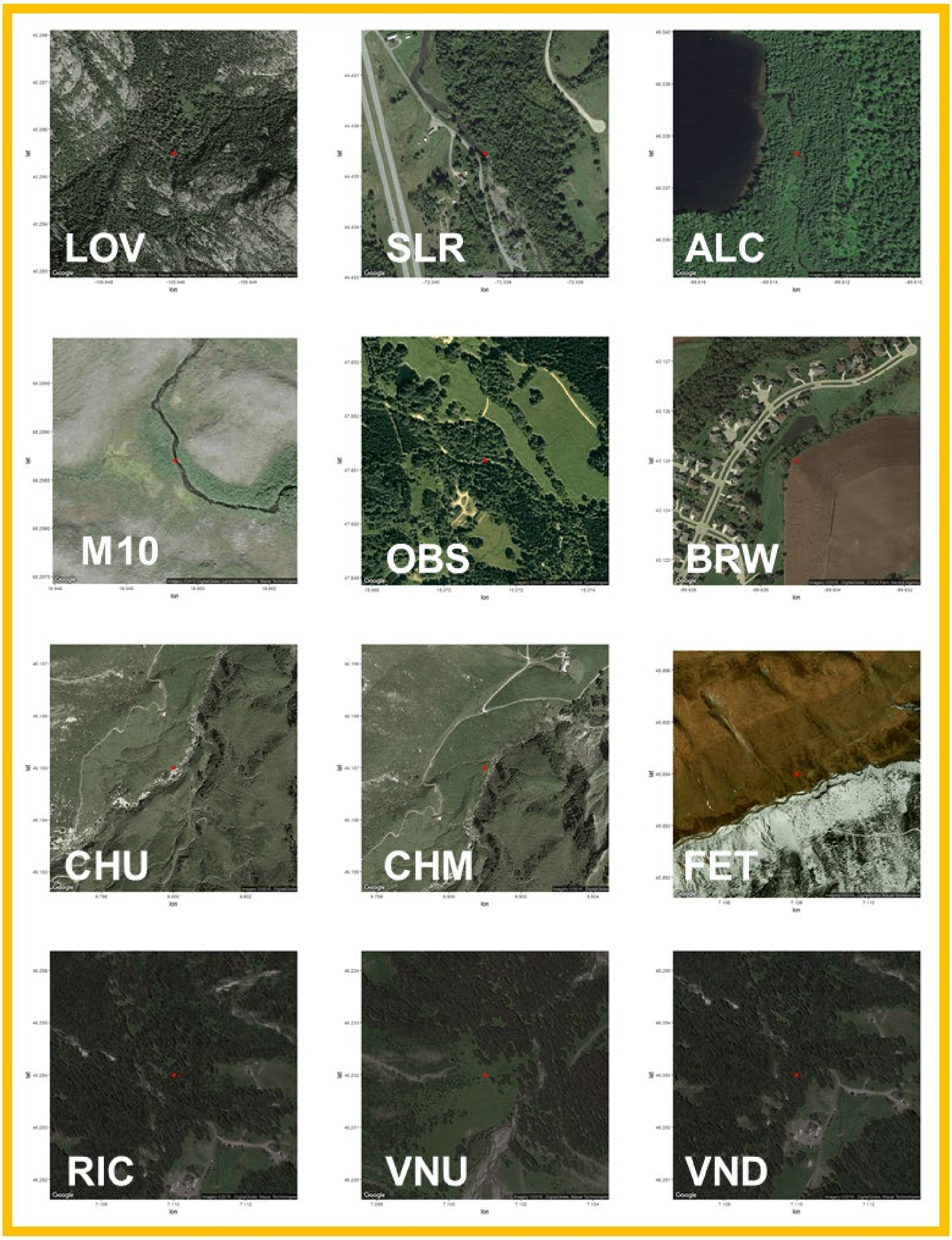

Figure S2a: Sites with the canopy cover category “no cover”, defined when the full extent of the stream was visible.

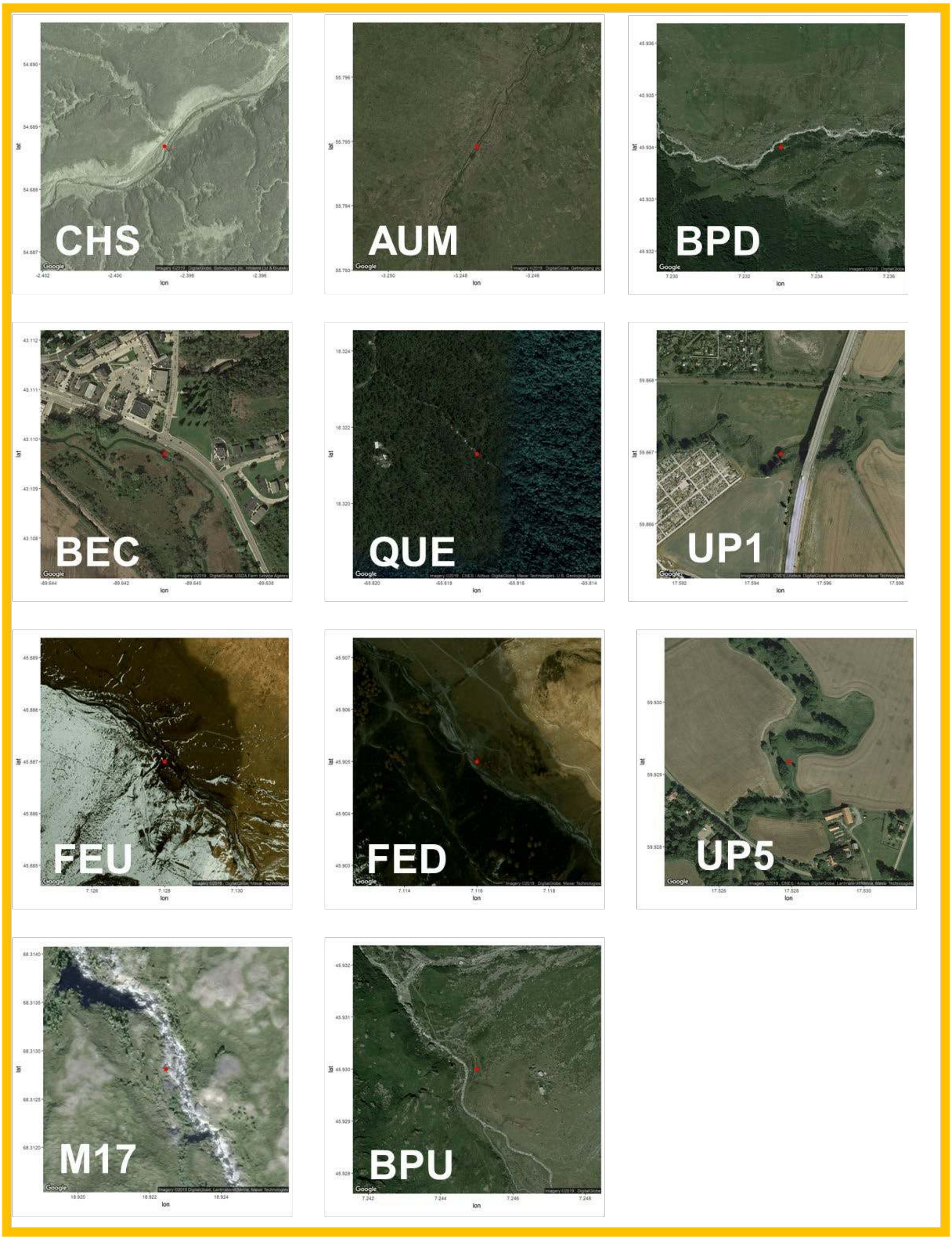

Figure S2a (cont.): Sites with the canopy cover category “no cover”, defined when the full extent of the stream was visible.

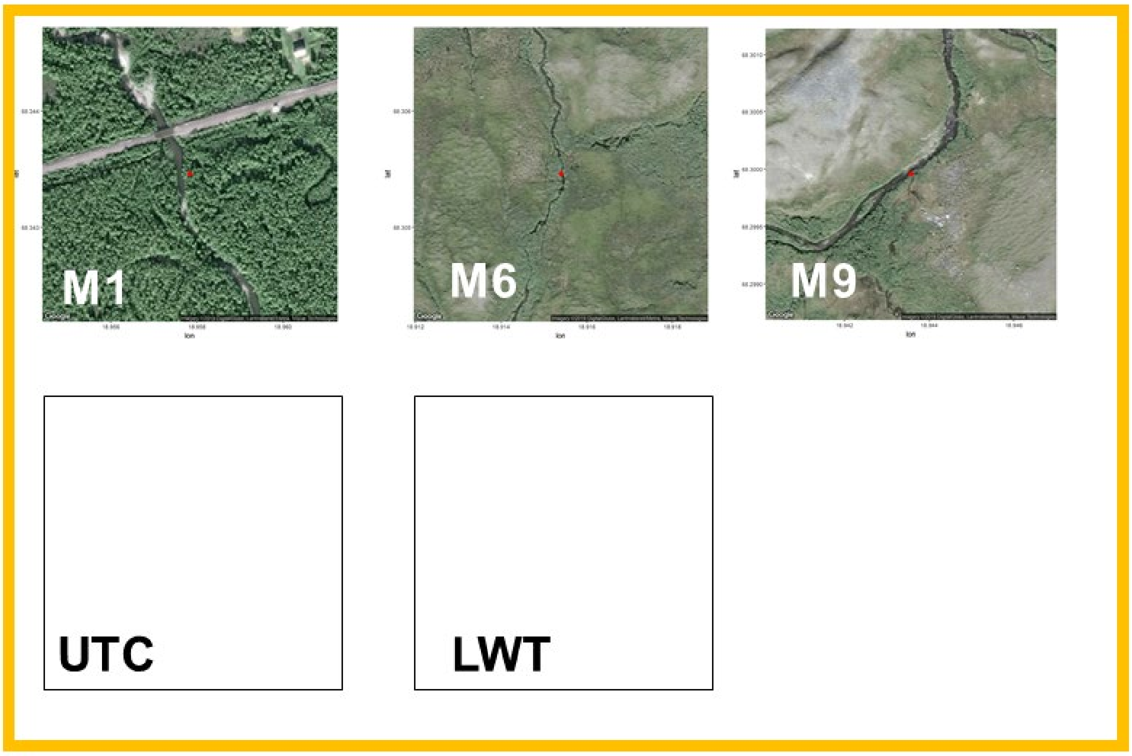

Figure S2a (cont.): Sites with the canopy cover category "no cover", defined when the full extent of the stream was visible. Sites UTC and LWT have no high-resolution imagery on google earth due to the remoteness of the location (Alaska), but are located in the transition between tundra and boreal zones and are canopy free.

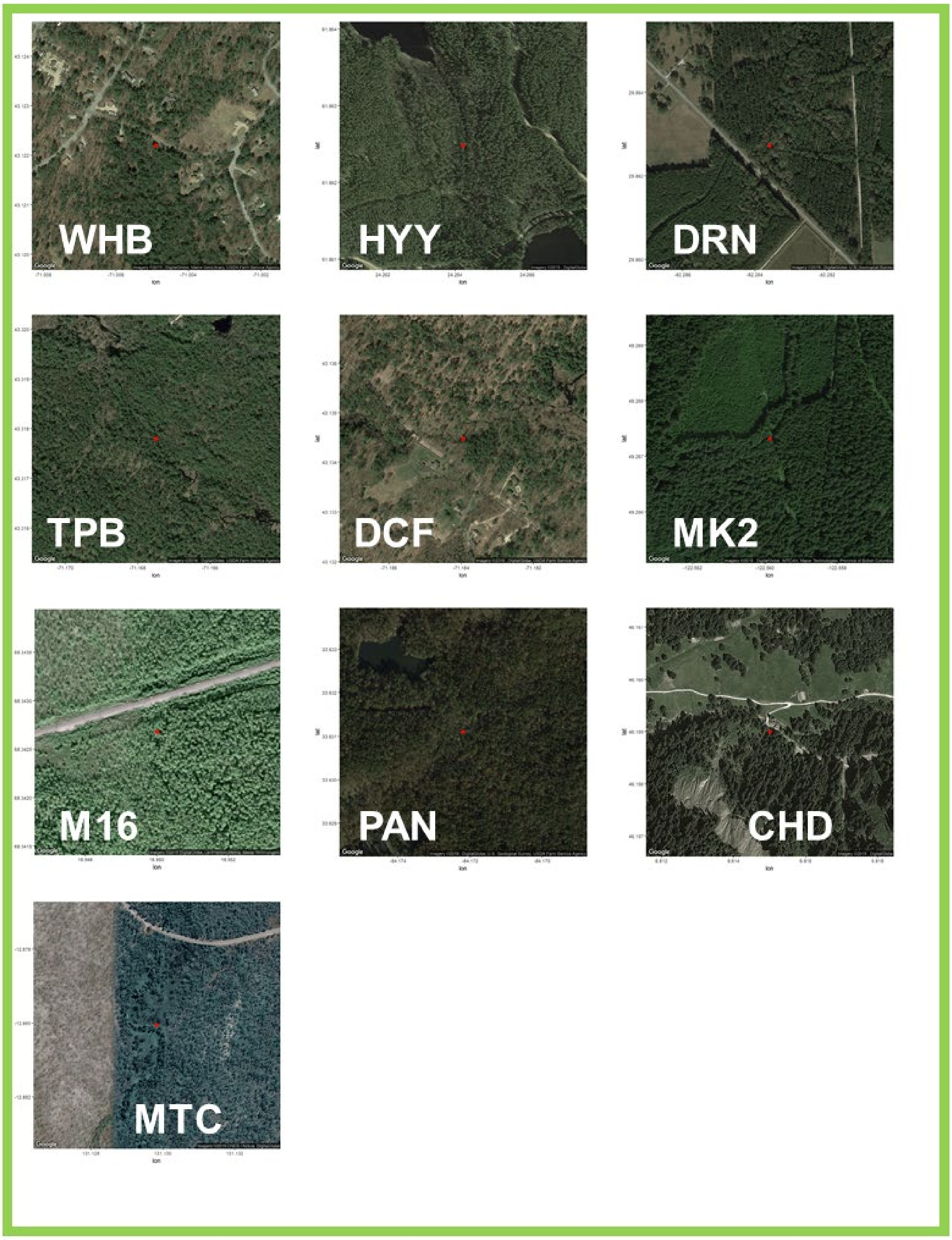

Figure S2b: Sites with the canopy cover category “partly covered, when it was possible to see multiple sections of the stream surface

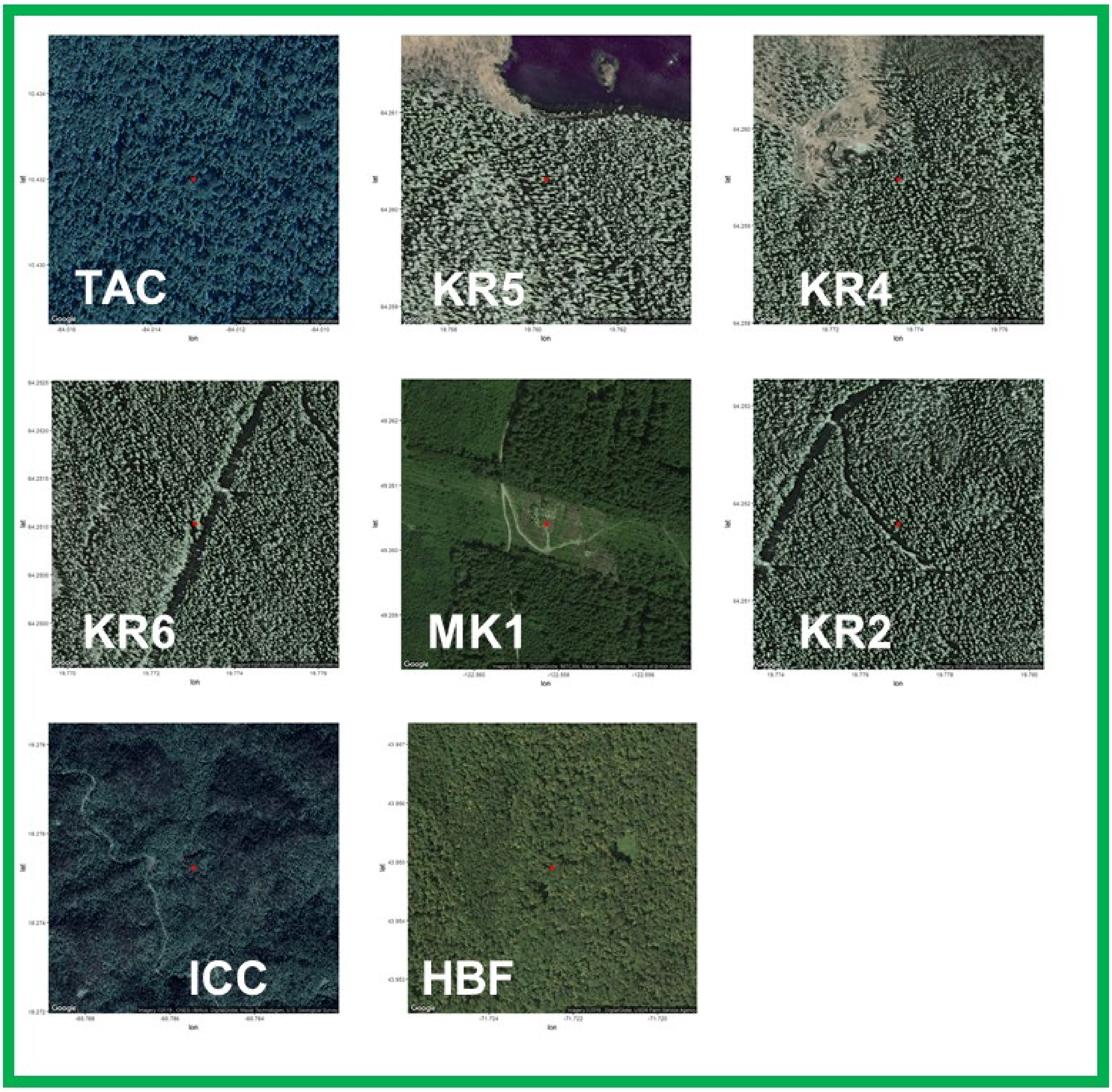

Figure S2c: Sites with the canopy cover category "fully covered", when the presence of a stream was not detectable from orthophotos.

S

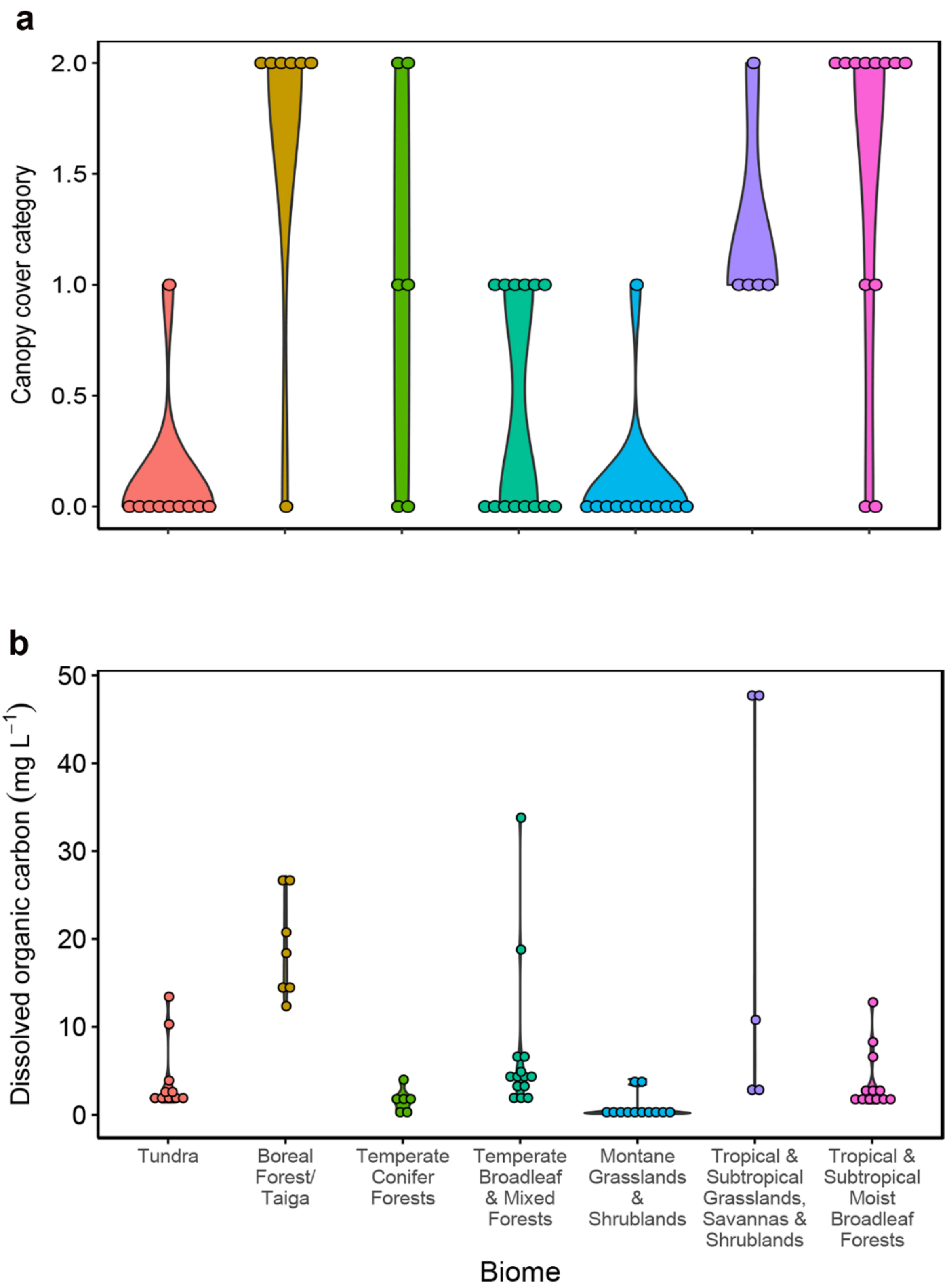

Figure S3. Ranges and distribution of canopy cover and stream DOC concentrations grouped by biome, and sorted by descending latitudes. Biome assignment derived from Olson et al. (2001)[3].

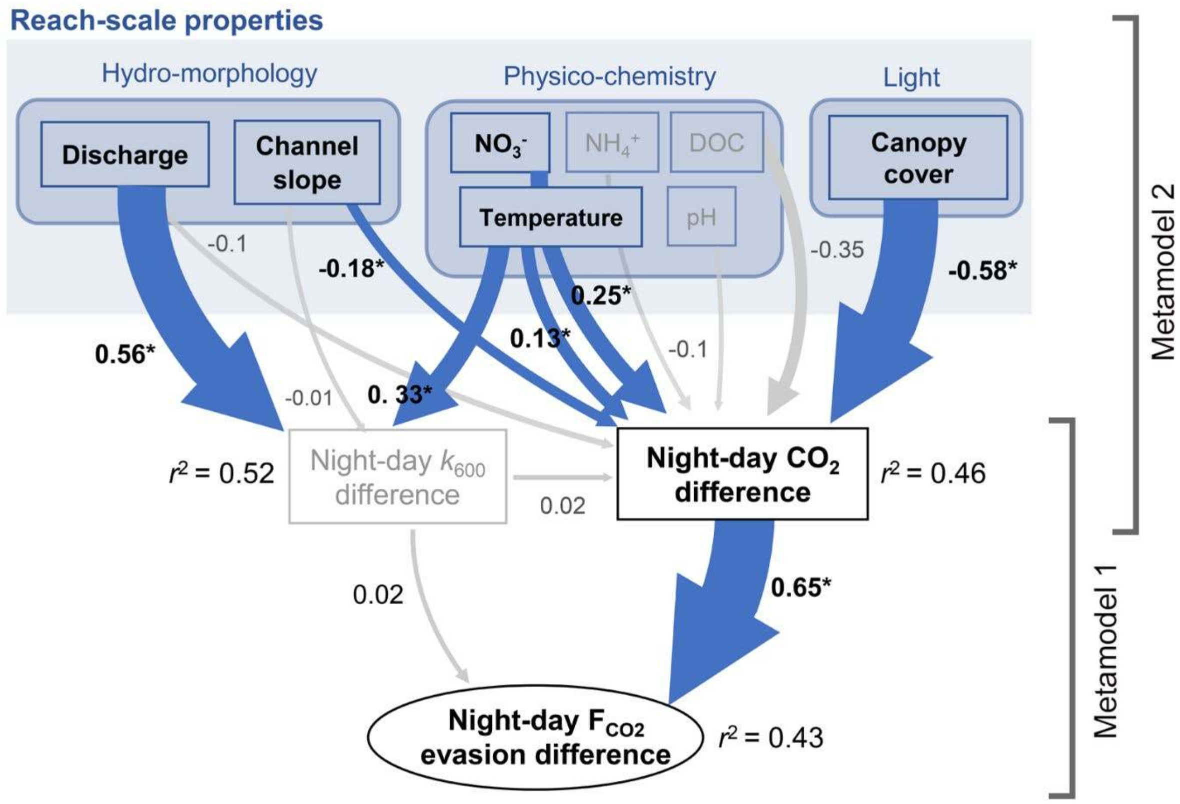

Figure S4. Drivers of night-day differences of CO_2 emissions from streams. Structural equation model (SEM) representing connections between reach-scale physical and biological parameters contributing to the relative night-day variation in summertime CO_2 emissions (%). The SEM consisted of two dependent levels of factor interaction or metamodels. Metamodel 1 assessed the influence of kCO_2 and stream water pCO_2 on night-day differences of CO_2 emissions. Metamodel 2 assessed relationships between environmental variables and diel changes in stream water pCO_2. Blue arrows represent significant effects ($p < 0.05$). Numbers adjacent to arrows are the standardized effect sizes of each relationship. Arrow width is proportional to the effect size. SEM goodness of fit was evaluated based on variance explained by each of the two models (r^2). A summary of statistical outputs from the SEM model is provided in Table S4. Reach-scale properties for each site used in the SEM model are presented in Table S2.

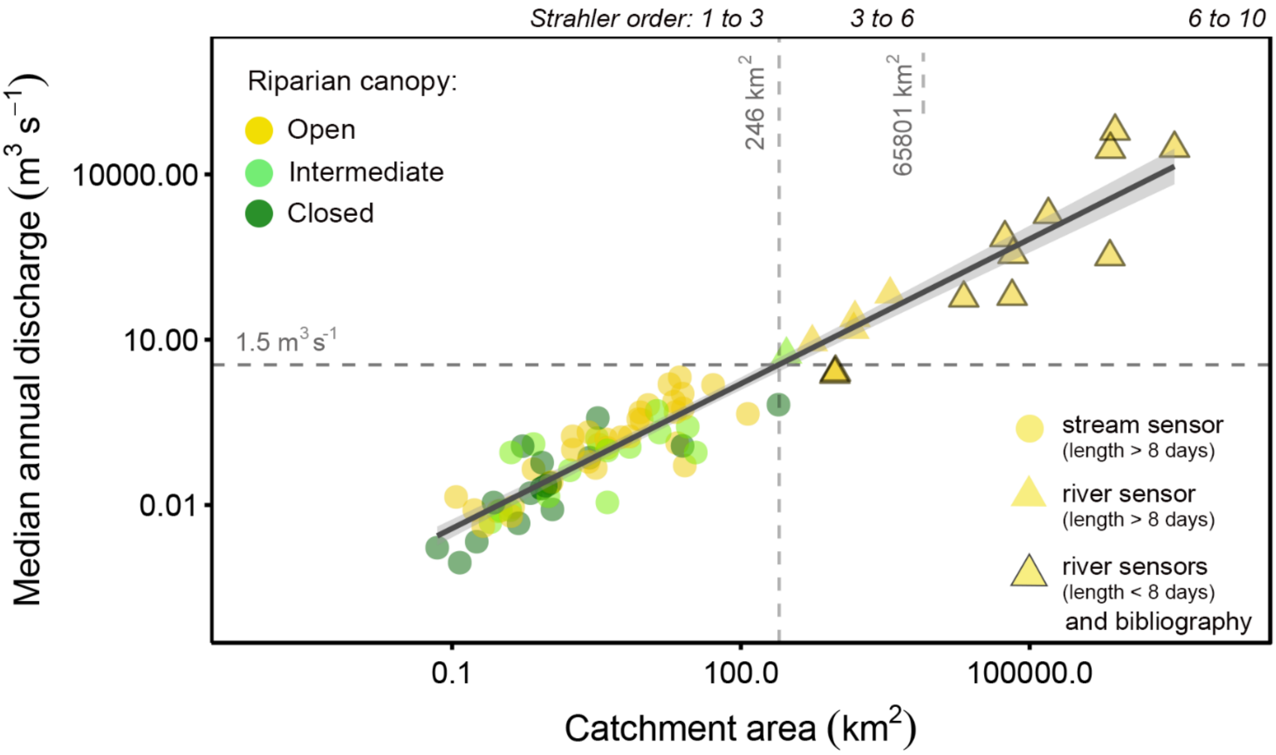

Figure S5. Distributions and relationship between catchment area and median annual discharge, colored by canopy color category. Symbols indicate the origin of the data (see Table S1 for more information). Strahler order obtained from the scaling ratio between catchment areas and river order by Guth, 2011[4].

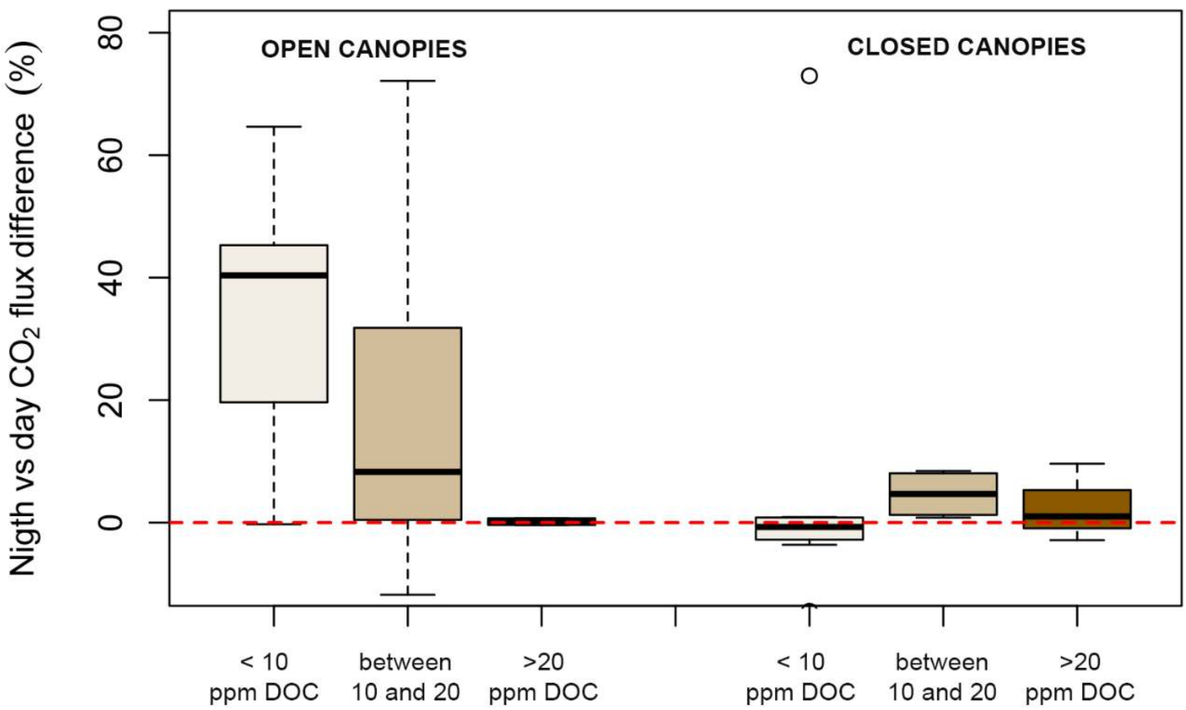

Figure S6. Comparison of night-day differences in CO_2 emission fluxes averaged by stream and grouped by canopy level and dissolved organic carbon concentration (DOC) level (lower than 10 ppm, between 10 and 20 ppm, and higher than 20 ppm). Box plots display the 25th, 50th, and 75th percentiles whiskers display minimum and maximum values.

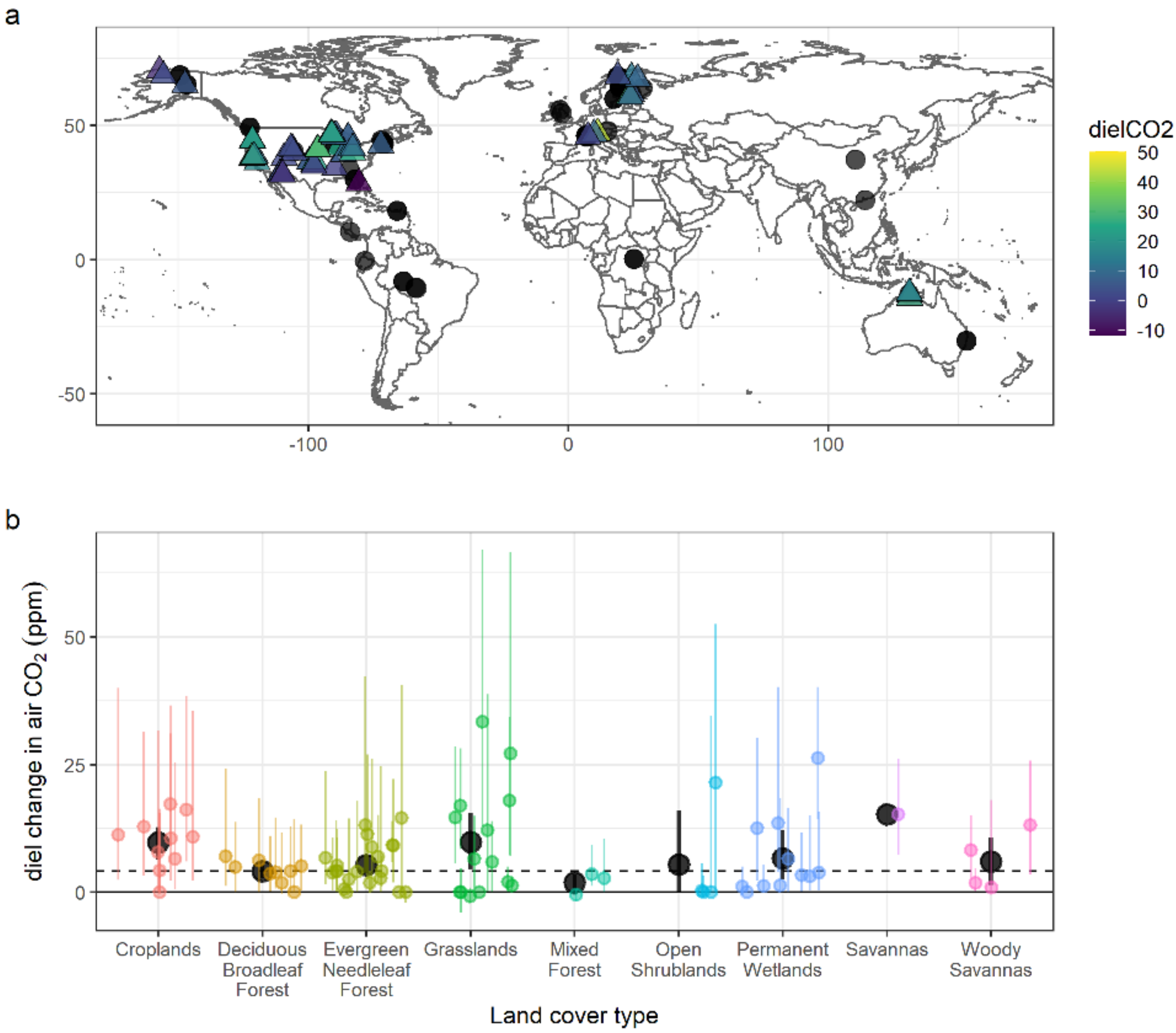

Figure S7: Night-day differences in atmospheric pCO_2 measured in eddy covariance towers in the FLUXNET network. Positive values indicate higher concentrations at night (average between 0 and 3h) than day (average between 12 and 15 h). a) shows the location of the towers (triangles) colored with the average amplitude, while the circles show the location of the stream sites in this study. b) shows the mean ± interquartile range for each site, grouped by land cover type. The black circle shows the median for each land cover. The dashed line shows the median of all values (4.2 ppm).

Supplementary Tables

Table S1. Summary of pCO_2 time series used to assess the daily bias on CO_2 evasion from streams.

Stream Id	Lat (°)	Long (°)	Altitude (m)	Country	Biome[a]	Source[b]	CO_2 sensor (model, manufacturer, country)	Initial date (yyyy-mm-dd)	Final date (yyyy-mm-dd)	Lenght (days)	Temporal resolution (min)
AFF	-9.8329	-55.9970	268	Brasil	TSMBF	3	GMM220, Vaisala, Finland	2017-03-07	2017-12-30	298	30
AFP	-9.8298	-55.9878	268	Brasil	TSMBF	3	GMM220, Vaisala, Finland	2017-06-29	2017-08-27	59	30
ALC	46.0377	-89.6133	494	USA	TBMF	1	GMM220, Vaisala, Finland	2014-04-08	2015-05-04	391	60
AUM	55.7949	-3.2476	266	Scotland	TBMF	1	GMM220, Vaisala, Finland	2007-11-21	2008-01-31	72	10
BAL	0.4228	25.1819	444	Congo	TSMBF	3	eosGP, Eosense, Canada	2019-04-04	2019-04-12	9	5
BEC	43.1097	-89.6408	268	USA	TBMF	2	GMM220, Vaisala, Finland	2016-07-19	2018-07-06	717	60
BPD	45.9340	7.2330	1937	Switzerland	TCF	3	GMM220, Vaisala, Finland	2016-09-30	2017-09-29	364	10
BPS	45.9280	7.2460	2161	Switzerland	TCF	3	GMM220, Vaisala, Finland	2016-09-30	2017-09-29	364	10
BPU	45.9300	7.2450	2148	Switzerland	TCF	3	GMM220, Vaisala, Finland	2016-09-30	2017-09-29	364	10
BRW	43.1250	-89.6350	278	USA	TBMF	2	GMM220, Vaisala, Finland	2016-08-10	2018-11-02	814	60
CAY	-0.3286	-78.2006	4093	Ecuador	MGS	1	GMM220, Vaisala, Finland	2019-07-12	2019-08-14	27	15
CHD	46.1590	6.8150	1415	Switzerland	TCF	3	GMM220, Vaisala, Finland	2016-09-30	2017-09-29	364	10
CHM	46.1570	6.8010	1630	Switzerland	TCF	3	GMM220, Vaisala, Finland	2016-09-30	2017-09-29	364	10
CHS	54.6887	-2.3986	601	UK	TBMF	1	GMM220, Vaisala, Finland	2009-05-25	2009-09-09	107	60
CHU	46.1550	6.8000	1689	Switzerland	TCF	3	GMM220, Vaisala, Finland	2016-09-30	2017-09-29	364	10
CU1	-8.0923	-63.4764	72	Brasil	TSMBF	3	EGM-4, PP-Systems, USA	2013-04-26	2013-05-04	8	10
CU2	-8.0851	-63.4806	75	Brasil	TSMBF	3	EGM-4, PP-Systems, USA	2013-04-26	2013-05-04	8	10
DCC	-30.1370	153.1636	42	Australia	TSGSS	3	LI-840, Licor, Germany	2019-01-29	2019-03-27	55	10
DCF	43.1345	-71.1840	101	USA	TBMF	2	K30, SenseAir, Sweden	2015-04-17	2017-09-12	879	60
DRN	29.8627	-82.2836	32	USA	TSGSS	2	eosGP, Eosense, Canada	2018-07-17	2019-05-28	315	60
FED	45.9050	7.1160	1774	Switzerland	TCF	3	GMM220, Vaisala, Finland	2016-09-30	2017-09-29	364	10
FET	45.8940	7.1080	2027	Switzerland	TCF	3	GMM220, Vaisala, Finland	2016-09-30	2017-09-29	364	10
FEU	45.8870	7.1280	1995	Switzerland	TCF	3	GMM220, Vaisala, Finland	2016-09-30	2017-09-29	364	10
HBF	43.9549	-71.7225	546	USA	TBMF	2	K30, SenseAir, Sweden	2015-05-14	2017-06-22	770	60
HEA	-30.1367	153.1898	5	Australia	TSGSS	3	LI-840, Licor, Germany	2018-03-07	2018-04-04	28	10
HKS	22.2668	114.1406	175	China	TSMBF	3	eosGP, Eosense, Canada	2020-11-17	2020-11-25	8	15
HYY	61.8625	24.2642	152	Finland	BFT	1	GMM220, Vaisala, Finland	2010-03-30	2010-10-27	211	60
ICC	18.2752	-65.7854	616	USA	TSMBF	1	GMM220, Vaisala, Finland	2014-03-13	2015-02-26	350	60
JU1	-10.4167	-58.7667	243	Brasil	TSMBF	1	GMM220, Vaisala, Finland	2005-03-31	2005-05-25	55	30
JU2	-10.4367	-58.4667	250	Brasil	TSMBF	1	GMM220, Vaisala, Finland	2005-03-31	2005-05-26	56	30
KR2	64.2518	19.7769	249	Sweden	BFT	3	GMM220, Vaisala, Finland	2012-08-30	2016-11-30	1553	60
KR4	64.2595	19.7736	297	Sweden	BFT	3	GMM220, Vaisala, Finland	2013-10-21	2016-12-01	1137	60
KR5	64.2603	19.7603	295	Sweden	BFT	3	GMM220, Vaisala, Finland	2013-12-06	2017-09-08	1372	60
KR6	64.2510	19.7731	238	Sweden	BFT	3	GMM220, Vaisala, Finland	2016-06-09	2016-11-30	174	60
KR7	64.2510	19.7731	168	Sweden	BFT	1	GMM220, Vaisala, Finland	2007-04-18	2008-05-09	387	60
KUP	68.6474	-149.4119	739	USA	T	3	eosGP, Eosense, Canada	2018-07-19	2018-08-01	13	10
LOV	40.2955	-105.6461	3215	USA	TCF	1	GMM220, Vaisala, Finland	2012-05-09	2012-11-02	177	60
LTC	65.3420	-146.9144	1525	USA	T	1	GMM220, Vaisala, Finland	2011-05-29	2011-09-25	119	60
M1	68.3435	18.9578	381	Sweden	T	3	GMM220, Vaisala, Finland	2016-08-03	2016-09-27	54	60
M6	68.3055	18.9154	747	Sweden	T	3	GMM220, Vaisala, Finland	2015-07-04	2016-09-08	149	60
M9	68.3000	18.9436	800	Sweden	T	3	GMM220, Vaisala, Finland	2015-07-04	2016-09-08	149	60
M10	68.2987	18.9494	815	Sweden	T	3	GMM220, Vaisala, Finland	2015-07-04	2016-09-08	149	60
M16	68.3427	18.9500	385	Sweden	T	3	GMM220, Vaisala, Finland	2016-05-27	2016-08-17	82	60
M17	68.3128	18.9225	706	Sweden	T	3	GMM220, Vaisala, Finland	2015-08-12	2016-08-16	87	60
MK1	49.2604	-122.5583	979	Canada	TCF	1	GMM220, Vaisala, Finland	2007-04-04	2008-07-10	463	60
MK2	49.2673	-122.5599	979	Canada	TCF	1	GMMP221, Vaisala, Finland	2016-11-05	2017-06-27	234	60
MTC	-12.8801	131.1298	48	Australia	TSGSS	3	eosGP, Eosense, Canada	2018-04-07	2019-03-21	348	5
OBS	47.8512	15.0711	617	Austria	TCF	1	GHG Sentinel, Axys, Canada	2010-05-01	2013-03-29	1063	180
PAN	33.6311	-84.1722	222	USA	TBMF	1	GMM220, Vaisala, Finland	2012-06-19	2013-05-14	329	60
QUE	18.3213	-65.8171	385	USA	TSMBF	2	K30, SenseAir, Sweden	2017-07-12	2017-12-20	161	60
RIC	46.2540	7.1100	1200	Switzerland	TCF	2	GMM220, Vaisala, Finland	2016-09-30	2017-09-29	364	10
SAF	29.8461	-82.2199	30	USA	TSGSS	3	eosGP, Eosense, Canada	2016-08-22	2018-01-03	499	60
SBM	43.1704	-71.2173	206	USA	TBMF	2	K30, SenseAir, Sweden	2015-04-13	2016-07-03	447	60
SLR	44.4354	-72.0385	524	USA	TBMF	1	GMM220, Vaisala, Finland	2012-04-20	2012-10-29	192	60
TAC	10.4320	-84.0130	46	Costa Rica	TSMBF	2	GMMP221, Vaisala, Finland	2013-04-01	2013-09-27	179	60
TOO	68.6468	-149.3192	741	USA	T	3	eosGP, Eosense, Canada	2018-07-19	2018-08-01	13	10
TPB	43.3178	-71.1675	192	USA	TBMF	2	K30, SenseAir, Sweden	2016-04-14	2017-10-25	559	60
UP1	59.8670	17.5948	33	Sweden	TBMF	3	K30, SenseAir, Sweden	2017-06-23	2017-08-12	50	30
UP5	59.9292	17.5279	32	Sweden	TBMF	3	K30, SenseAir, Sweden	2017-06-22	2017-08-13	52	30
UTC	65.3515	-146.9073	1525	USA	T	1	GMM220, Vaisala, Finland	2011-05-18	2011-09-25	130	60
VAL	63.8667	28.6667	198	Finland	BFT	1	GMM220, Vaisala, Finland	2008-04-10	2008-06-01	52	10
VND	46.2530	7.1100	1201	Switzerland	TCF	3	GMM220, Vaisala, Finland	2016-09-30	2017-09-29	364	10
VNU	46.2320	7.1010	1465	Switzerland	TCF	3	GMM220, Vaisala, Finland	2016-09-30	2017-09-29	364	10
WHB	43.1222	-71.0049	31	USA	TBMF	2	K30, SenseAir, Sweden	2015-04-23	2017-10-31	922	60
YEL	37.2310	110.4099	730	China	MGS	3	eosGP, Eosense, Canada	2019-08-29	2019-09-15	17	10
YOK	0.2935	25.2950	440	Congo	TSMBF	3	eosGP, Eosense, Canada	2019-04-03	2019-05-08	35	5

[a] Biome assignment derived from *Olson et al*. (2001)[3]:

T= Tundra
BFT= Boreal Forest/Taiga
TCF= Temperate Conifer Forests
TBM= Temperate Broadleaf & Mixed Forests
MGS= Montane Grasslands & Shrublnads
TSGSS= Tropical & Subtropical Grasslands, Savannas & Shrublands
TSMBF= Tropical & Subtropical Moist Broadleaf Forests

[b] 1=Literature dataset, 2=StreamPulse dataset, 3=Unpublished dataset

Table S2. Summary of reach-, catchment- and regional-scale properties of the study sites.

	Stream reach properties									Catchment prpoerties					Regional prpoerties	
Stream Id	Riparian canopy	Channel slope	Median discharge	Water temp.	pH	Cond.	[DOC]	$[NO_3^-]$	$[NH_4^+]$	Area	Mineral surfaces	Grass and Shrubs	Crops	Forest	MAT	MAP
	Category	m m^{-1}	L s^{-1}	°C		µS cm^{-1}	mg L^{-1}	µg L^{-1}	µg L^{-1}	km^2	%	%	%	%	°C	mm
AFF	1	0.005	284.0	25.6	6.6	80.2	3.0	NA	18.8	13.1						
AFP	0	0.003	25.9	27.4	6.0	54.8	2.2	NA	16.2	1.5						
ALC	0	0.003	132.5	8.7	7.0	55.0	4.9	20.0	43.0	21.8	0	100	0	0	4.1	673
AUM	0	0.004	51.2	4.4	5.5	87.8	33.8	NA	57.1	3.4	0	100	0	0	7.5	746
BAL	2	0.002	75.4	25.0	6.6	25.0	12.8	110.0	70.0	2.7						
BEC	0	0.004	446.3	10.1	8.0	610.0	4.8	2750.0	103.5	118.1	0	46	0	22	7.6	687
BPD	0	0.108	1534.8	3.7	8.1	166.7	0.2	121.7	12.6	23.2	11	76	0	13	1.8	1359
BPS	0	0.043	52.0	3.9	8.1	151.6	0.4	79.7	2.7	3.1	11	89	0	0	1.1	1501
BPU	0	0.035	764.1	2.4	8.1	183.9	0.2	124.8	15.8	18.1	0	100	0	0	1.1	1501
BRW	0	0.001	46.6	9.8	8.0	610.0	6.5	3250.0	55.0	26.2	0	34	50	16	7.6	687
CAY	0	0.013	227.0	6.5	6.6	83.1	4.1	5.0	0.5	0.4						
CHD	1	0.123	50.6	5.8	8.4	599.2	0.5	146.5	7.5	3.2	0	47	0	53	4.4	1297
CHM	0	0.223	5.7	4.6	8.3	305.2	0.4	56.4	7.2	0.7	0	95	0	5	3.9	1333
CHS	0	0.025	7.5	11.5	4.3	41.8	18.8	NA	43.6	0.2	0	100	0	0	6.1	1505
CHU	0	0.167	29.3	5.3	8.3	335.1	0.4	58.4	8.7	0.3	0	100	0	0	3.9	1333
CU1	2	0.013	47.7	25.3	5.6	42.2	2.5	1.1	29.3	1.0						
CU2	2	0.013	44.2	25.7	6.3	67.8	8.3	1.4	8.9	0.9						
DCC	1	0.017	64.0	22.3	6.6	491.0	3.1	5040.0	19.0	0.2						
DCF	1	0.014	100.4	15.6	6.1	50.0	6.8	49.0	19.0	7.0	0	0	0	100	7.8	884
DRN	1	0.003	668.5	19.0	4.4	55.0	47.7	12.0	142.0	34.0	0	0	25	100	20.3	1102
FED	0	0.100	223.4	3.8	8.3	343.0	0.2	108.0	4.0	20.2	0	59	0	41	2.6	1344
FET	0	0.046	354.3	5.8	8.3	439.7	0.2	70.8	4.5	4.0	0	87	0	13	1.0	1640
FEU	0	0.061	6.2	4.8	8.2	265.6	0.1	97.9	5.0	9.3	0	100	0	0	1.8	1453
HBF	2	0.183	42.7	11.9	5.7	11.0	2.8	82.0	6.0	0.4	0	0	0	100	5.2	974
HEA	1	0.023	57.4	22.7	6.8	93.5	10.8	672.0	33.8	1.7						
HKS	2	0.097	174.9	26.8	6.6	83.1	1.5	154.0	26.0	4.1						
HYY	0	0.010	294.3	13.1	6.5	32.0	14.1	10.0	38.2	7.0	0	0	0	25	3.3	551
ICC	2	0.021	74.5	21.1	6.5	57.0	1.7	149.0	8.0	3.3	0	0	0	100	21.1	1707
JU1	2	0.013	47.7	24.4	6.1	48.8	2.3	NA	16.4	1.0						
JU2	2	0.013	1.0	24.9	6.4	71.9	2.7	NA	17.9	0.9						
KR2	2	0.031	2.0	2.1	5.0	34.4	18.4	16.1	34.0	0.1	0	0	0	100	1.8	518
KR4	2	0.040	7.6	4.1	4.8	53.1	27.1	65.3	46.5	0.2	0	44	0	100	1.6	520
KR5	2	0.008	8.0	5.3	5.0	36.3	14.9	39.7	46.1	0.7	0	0	0	100	1.6	523
KR6	2	0.073	5.7	4.2	5.5	32.6	12.4	72.1	34.3	1.1	0	0	0	100	1.7	516
KR7	2	0.005	4.2	5.8	4.9	25.4	20.8	34.4	16.6	0.5	0	0	0	100	1.9	503
KUP	0	0.009	175.4	9.3	7.2	47.0	3.9	80.0	2.0	0.2						
LOV	0	0.101	109.9	9.0	6.4	13.0	1.6	1100.0	20.0	1.8	0	100	0	0	1.1	479
LTC	0	0.034	108.9	3.9	6.4	27.6	13.4	168.0	28.0	4.1	0	100	0	0	-4.6	269
M1	0	0.005	333.3	7.6	7.0	38.1	2.5	40.0	17.2	51.5	0	106	0	15	0.3	295
M6	0	0.078	165.2	6.7	7.0	24.4	1.6	34.0	14.0	1.8	0	79	0	21	-1.9	421
M9	0	0.034	12.7	5.7	7.2	33.2	1.6	27.0	14.0	10.9	0	100	0	0	-2.2	455
M10	0	0.028	106.3	6.0	7.1	21.8	2.7	28.0	17.9	8.6	0	100	0	0	-2.2	455
M16	1	0.011	788.5	5.9	7.0	21.8	1.8	91.0	14.8	0.7	0	51	0	49	0.3	295
M17	0	0.010	1.7	7.8	6.9	43.2	2.4	9.0	16.9	0.1	0	83	0	17	-1.6	396
MK1	2	0.035	115.9	8.1	5.7	22.2	4.0	NA	21.4	0.1	0	0	0	100	9.1	1867
MK2	2	0.035	265.6	7.1	6.9	12.0	2.0	NA	15.6	0.5	0	0	0	100	9.2	1880
MTC	1	0.009	1089.9	27.2	7.7	454.0	2.6	65.0	71.0	28.0	0	16	0	84	27.2	1203
OBS	0	0.008	77.6	6.7	8.3	232.0	1.7	570.0	4.0	24.8	0	95	0	5	7.1	797
PAN	1	0.024	362.9	14.6	6.2	33.8	3.7	120.0	171.5	0.4	0	0	0	100	16.4	1065
QUE	0	0.223	228.7	22.7	7.2	52.0	1.9	155.0	7.0	2.6	0	75	0	25	23.0	1769
RIC	1	0.153	702.2	4.1	8.6	239.3	0.4	188.7	5.0	14.3	0	50	0	50	5.6	1078
SAF	2	0.002	661.4	19.3	5.3	96.0	47.7	64.0	150.0	245.8	0	0	25	100	20.2	1103
SBM	1	0.047	5.7	10.9	4.6	30.0	1.9	9.0	7.0	0.3	0	0	0	100	7.4	907
SLR	0	0.011	8.5	12.1	7.7	150.6	1.7	84.0	14.2	0.4	0	29	0	71	5.9	814
TAC	2	0.031	157.6	24.6	5.4	22.3	1.3	1333.0	29.8	0.3	0	0	0	100	26.0	3174
TOO	0	0.003	64.4	12.7	6.6	20.0	10.3	NA	7.6	5.7						
TPB	1	0.021	81.5	14.2	5.0	18.0	4.2	16.0	10.0	4.1	0	0	0	100	7.0	918
UP1	0	0.010	165.0	15.2	7.8	580.0	4.4	310.0	25.0	25.0	10	115	60	0	5.8	467
UP5	0	0.013	61.4	15.1	8.1	670.0	2.2	2690.0	22.0	21.0	0	109	77	0	5.7	474
UTC	0	0.036	50.7	2.8	6.7	102.0	1.4	581.0	28.0	2.6	0	100	0	0	-4.5	271
VAL	2	0.021	477.7	7.5	4.3	31.8	26.2	8.0	8.7	0.9	0	0	0	100	1.7	522
VND	1	0.107	446.6	4.6	8.6	216.6	0.2	171.1	3.7	13.4	0	85	0	25	5.6	1078
VNU	0	0.028	9.6	4.6	8.2	209.2	0.1	168.0	2.8	9.0	0	63	0	37	4.6	1134
WHB	1	0.016	47.0	13.3	7.0	343.0	3.9	710.0	12.0	1.0	0	0	0	100	8.2	896
YEL	0	0.006	24.4	20.1	8.6	1127.0	3.5	NA	20.0	1.1						
YOK	2	0.008	22.4	24.4	6.7	29.8	6.6	233.0	47.0	0.9						

Table S3. Summary of stream diel CO_2 concentration and flux patterns.

Stream Id	CO_2 concentration (ppm)				CO_2 flux (g C m^{-2} d^{-1})				
	Day-time	Night-time	Diff.	(%)	Day-time	Night-time	Diff.	(%)	Night > day (%)
AFF	7319	7407	87.8	1.2	12.8	12.9	0.1	0.7	60.5
AFP	7139	6444	-694.2	-9.7	6.9	6.2	-0.7	-5.0	25.0
ALC	2176	2560	383.8	17.6	2.5	3.1	0.6	33.0	80.6
AUM	4087	4013	-73.9	-1.8	5.4	5.3	-0.1	0.1	34.5
BAL	2974	3126	151.7	5.1	2.5	2.8	0.2	8.4	77.8
BEC	2351	3260	909.4	38.7	3.5	5.2	1.7	59.8	87.7
BPD	392	402	9.7	2.5	-0.7	-0.3	0.4	13.4	37.5
BPS	520	546	25.1	4.8	0.6	0.9	0.3	192.5	97.6
BPU	380	399	18.2	4.8	-0.4	0.0	0.4	-11.8	26.5
BRW	6268	7288	1020.4	16.3	6.1	7.3	1.2	31.6	77.6
CAY	2716	3831	1115.4	41.1	4.2	6.4	2.2	68.2	96.3
CHD	667	679	12.5	1.9	7.2	7.4	0.2	15.8	48.3
CHM	507	491	-16.7	-3.3	4.2	3.4	-0.8	32.8	81.0
CHS	5201	6626	1425.1	27.4	9.4	12.6	3.1	40.2	98.0
CHU	473	519	45.9	9.7	0.8	1.3	0.5	80.1	89.0
CU1	8812	8677	-135.5	-1.5	71.2	70.7	-0.5	-0.7	20.0
CU2	10812	10698	-113.2	-1.0	87.9	87.4	-0.5	-3.6	0.0
DCC	4058	4274	215.7	5.3	6.3	7.0	0.7	10.8	96.4
DCF	1347	1587	239.7	17.8	2.0	2.5	0.5	31.9	96.1
DRN	8208	8245	37.7	0.5	15.4	15.4	-0.1	11.1	59.8
FED	442	449	6.8	1.5	1.4	1.9	0.5	45.1	66.4
FET	487	504	17.5	3.6	0.8	1.0	0.1	31.7	72.6
FEU	825	858	33.0	4.0	7.3	9.6	2.3	30.0	92.3
HBF	737	830	93.3	12.6	2.5	3.5	1.0	55.1	84.6
HEA	4218	4963	744.7	17.7	9.2	11.2	2.0	24.7	88.9
HKS	583	700	116.6	20.0	9.4	16.3	6.9	80.3	87.5
HYY	1317	1517	199.5	15.1	2.2	2.7	0.4	66.8	88.4
ICC	2979	2977	-2.3	-0.1	10.8	10.8	0.0	0.9	65.9
JU1	3311	3182	-128.7	-3.9	24.9	24.0	-0.9	-4.5	30.6
JU2	6105	6015	-90.6	-1.5	48.7	47.9	-0.8	-1.3	36.2
KR2	7361	7535	174.1	2.4	13.3	14.2	0.9	8.4	81.0
KR4	8137	8173	35.5	0.4	17.8	18.0	0.1	1.0	51.2
KR5	3650	3659	8.6	0.2	5.2	5.3	0.2	0.8	52.1
KR6	1886	1901	15.0	0.8	7.8	7.9	0.1	1.7	55.7
KR7	1765	1873	107.7	6.1	1.8	1.9	0.1	10.4	89.1
KUP	895	952	57.4	6.4	0.7	0.8	0.1	12.9	92.3
LOV	596	807	211.7	35.5	4.9	9.7	4.9	145.2	98.8
LTC	1350	1478	128.4	9.5	5.6	6.5	0.9	17.7	91.7
M1	1008	1283	274.7	27.3	1.5	2.3	0.8	53.5	94.5
M6	681	749	68.0	10.0	1.8	2.2	0.5	39.1	77.5
M9	1442	1573	130.9	9.1	2.5	2.9	0.4	14.8	92.8
M10	2292	2530	237.8	10.4	3.4	3.9	0.5	13.6	88.6
M16	808	824	16.6	2.1	6.1	6.4	0.2	3.3	63.8
M17	822	950	128.6	15.7	4.5	6.0	1.5	34.5	98.0
MK1	2825	2843	18.2	0.6	4.9	4.9	0.0	1.1	58.0
MK2	1454	1437	-17.6	-1.2	6.0	5.9	-0.1	-1.2	54.1
MTC	5718	5693	-25.9	-0.5	11.1	11.1	0.0	0.8	48.2
OBS	559	851	292.2	52.3	0.4	1.1	0.7	143.8	97.7
PAN	5466	5368	-98.2	-1.8	16.0	16.0	0.0	1.2	56.1
QUE	1447	1371	-76.2	-5.3	72.2	68.5	-3.7	-5.8	23.9
RIC	458	472	14.8	3.2	2.3	3.3	1.0	43.1	91.1
SAF	6469	5754	-715.6	###	6.6	6.3	-0.3	-3.2	29.7
SBM	3236	3339	103.7	3.2	10.5	9.9	-0.6	3.1	60.9
SLR	1589	1626	37.3	2.4	1.5	1.6	0.1	4.2	50.0
TAC	6480	6641	160.8	2.5	12.7	13.2	0.5	1.2	72.2
TOO	1700	2077	376.9	22.2	1.8	2.3	0.5	29.2	88.9
TPB	1750	1892	142.5	8.1	4.4	4.9	0.5	12.6	87.7
UP1	6484	7990	1505.8	23.2	33.7	44.1	10.4	34.3	98.0
UP5	3991	5005	1014.3	25.4	31.4	42.9	11.5	37.7	94.3
UTC	2362	2745	383.7	16.2	10.4	12.8	2.3	21.8	95.4
VAL	4718	4942	223.4	4.7	10.9	11.5	0.5	5.7	81.0
VND	454	463	9.5	2.1	1.9	2.4	0.5	22.8	80.9
VNU	592	603	11.7	2.0	1.5	1.6	0.1	9.0	82.5
WHB	1287	1434	146.2	11.4	1.7	2.0	0.4	24.9	89.3
YEL	1283	1968	685.0	53.4	2.9	5.3	2.4	84.6	94.4
YOK	1944	1860	-84.2	-4.3	2.4	2.3	0.0	-1.9	32.1
Mean	**2915**	**3087**	**172.1**	**9.0**	**10.7**	**11.6**	**0.9**	**27.2**	**72.3**

Table S4. Summary of the structural equation model (SEM) statistical outputs.

Model	Response	Predictors	Std. Estimate	*p-value*	R^2	RSE
1	Δ CO_2 Flux	**Δ *p*CO_2**	**0.65 *****	**< 0.001**	0.43	38.3
		Δ *k*CO_2	0.02	0.56		
2	Δ *p*CO_2	**Canopy cover**	**-0.58 *****	**< 0.001**	0.46	15.9
		[DOC]	-0.35	0.75		
		[NO_3^-]	**0.25 ***	**< 0.001**		
		Channel slope	**-0.18 ***	**< 0.001**		
		Δ Temperature	**0.13 ***	**< 0.001**		
		Δ Discharge	-0.10	0.31		
		Δ *k*CO_2	0.02	0.82		
		[NH_4^+]	0.10	0.45		
		pH	0.10	0.34		
3	Δ *k*CO_2	**Δ Discharge**	**0.56 *****	**< 0.001**	0.52	5.5
		Δ Temperature	**0.33 *****	**< 0.001**		
		Slope	-0.01	0.85		

Table S5. Summary of pCO_2 sensor time-series and literature data used to assess the daily bias on CO_2 evasion from larger rivers (see Figure 2 and Figure S5).

River id	Lat (°)	Long (°)	Altitude (m)	Country	Biome[a]	Data type[b]	Source	Canopy category	DOC ($mg\ L^{-1}$)[c]
Santa Fe (1500)	29.9526	-82.7863	17	USA	TSGSS	1	*Unpublished*	0	38.3
Santa Fe (2500)	29.9980	-82.2742	16	USA	TSGSS	1	*Unpublished*	0	11.9
Santa Fe (2800)	29.8493	-82.7148	10	USA	TSGSS	1	*Unpublished*	0	10.3
Ichetucknee River	29.9118	-82.8606	8	USA	TSGSS	1	*Unpublished*	0	1.0
New River	29.9219	-82.4262	27	USA	TSGSS	1	*Unpublished*	1	43.4
Colorado River (Cameo)	39.2390	-108.2660	1475	USA	DXS	2	*Unpublished*	0	3.1
Colorado River (Potash)	38.5050	-109.6580	1211	USA	DXS	2	*Unpublished*	0	3.5
Fluvià River (Armentera)	42.1685	3.0250	13	Spain	MFWS	2	*Unpublished*	0	0.9
Fluvià River (Pescador)	42.1769	3.0598	7	Spain	MFWS	2	*Unpublished*	0	0.9
Negro River	-3.1000	-60.1167	46	Brasil	TSMBF	2	*Unpublished*	0	8.6
Curuá River	1.7482	-51.4405	126	Brasil	TSMBF	2	*Unpublished*	0	4.2
Mississippi	30.4336	-91.1975	6	USA	TBMF	3	*Reiman and Xu., 2019*	0	6.3
Clark Fork (Missoula)	46.8668	-113.9903	988	USA	TBMF	3	*Lynch et al., 2010*	0	5.0
Zambezi River (mouth)	16.0162	28.8798	371	Mozambique	TSMBF	3	*Teodoru et al., 2015*	0	3.4
Congo River	-3.9495	15.9073	5	Congo	TSMBF	3	*Borges et al., 2019*	0	8.1
Red River	21.7000	104.8667	5	Vietnam	TSMBF	3	*Le et al., 2018*	0	2.1

[a] Biome assignment derived from *Olson et al*. (2001[3]):

T= Tundra
BFT= Boreal Forest/Taiga
TCF= Temperate Conifer Forests
TBM= Temperate Broadleaf & Mixed Forests
TGSS= Temperate Grasslands, Savannas & Shrublands
TSMBF= Tropical & Subtropical Moist Broadleaf Forests
TSGSS= Tropical & Subtropical Grasslands, Savannas & Shrublands

[b] Data type and origin

1. Sensor (long time-series, > 8 days)
2. Sensor (short time-series, < 8 days)
3. Extracted from the literature (non-continuous)[5–9]

References

1. Brooks, J. R., Flanagan, L. B., Varney, G. T. & Ehleringer, J. R. Vertical gradients in photosynthetic gas exchange characteristics and refixation of respired CO2 within boreal forest canopies. *Tree Physiology* **17**, 1–12 (1997).

2. Pastorello, G. The FLUXNET2015 dataset and the ONEFlux processing pipeline for eddy covariance data. 27.

3. Olson, D. M. *et al.* Terrestrial Ecoregions of the World: A New Map of Life on Earth. *BioScience* **51**, 933 (2001).

4. Guth, P. L. Drainage basin morphometry: a global snapshot from the shuttle radar topography mission. *Hydrol. Earth Syst. Sci.* **15**, 2091–2099 (2011).

5. Reiman, J. & Xu, Y. J. Diel Variability of pCO2 and CO2 Outgassing from the Lower Mississippi River: Implications for Riverine CO2 Outgassing Estimation. *Water* **11**, 43 (2018).

6. Lynch, J. K., Beatty, C. M., Seidel, M. P., Jungst, L. J. & DeGrandpre, M. D. Controls of riverine CO2 over an annual cycle determined using direct, high temporal resolution pCO2 measurements. *J. Geophys. Res.* **115**, G03016 (2010).

7. Teodoru, C. R. *et al.* Dynamics of greenhouse gases (CO₂, CH₄, N₂O) along the Zambezi River and major tributaries, and their importance in the riverine carbon budget. *Biogeosciences* **12**, 2431–2453 (2015).

8. Borges, A. V. *et al.* Variations in dissolved greenhouse gases (CO₂, CH₄, N₂O) in the Congo River network overwhelmingly driven by fluvial-wetland connectivity. *Biogeosciences* **16**, 3801–3834 (2019).

9. Le, T. P. Q. *et al.* CO₂ partial pressure and CO₂ emission along the lower Red River (Vietnam). *Biogeosciences* **15**, 4799–4814 (2018).

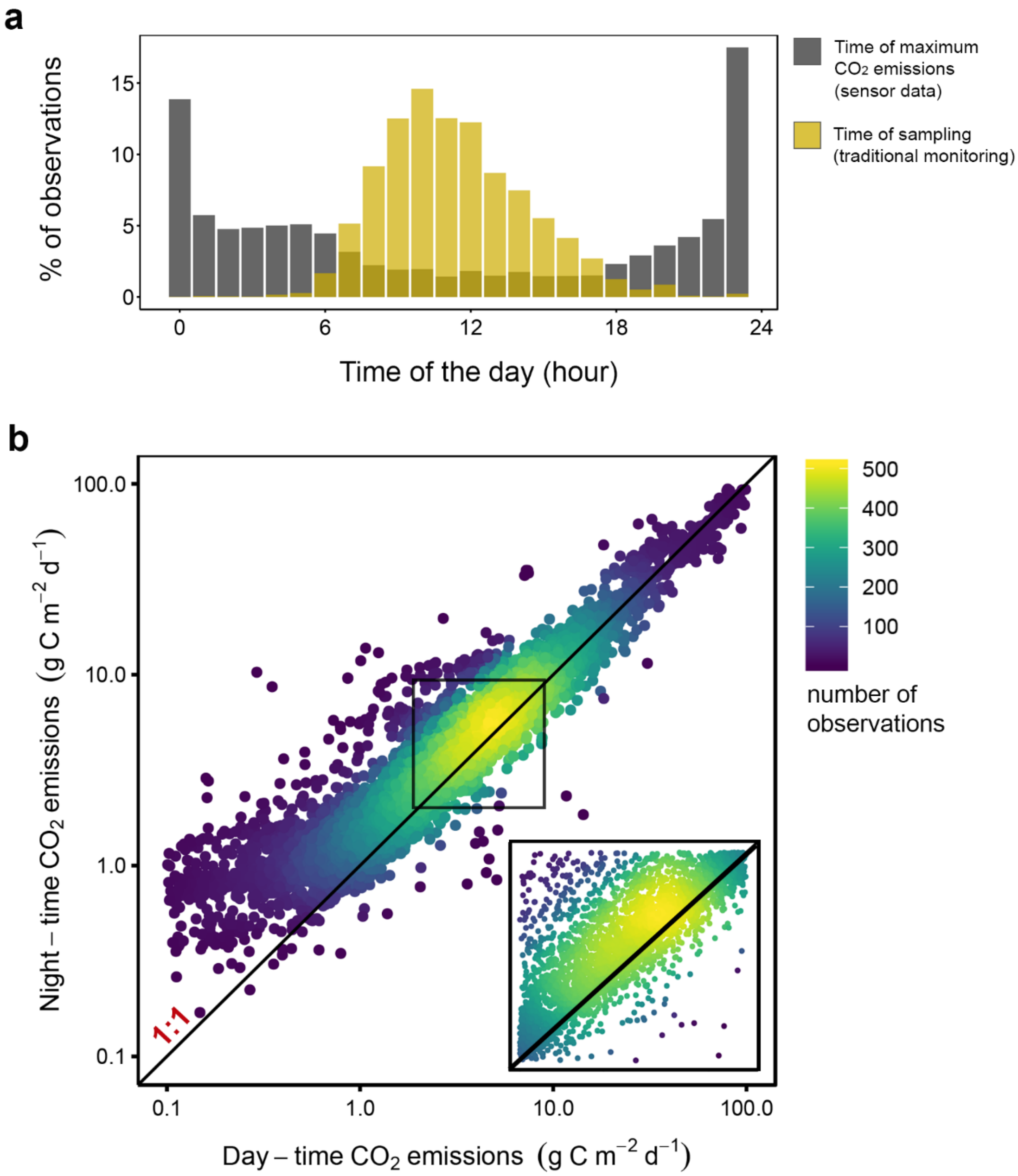

Figure 1. Magnitude and bias of diel variation in CO_2 emissions from global streams.

a) Distributions of observations of sampling time (GLORICH database[2]) and the time of maximum CO_2 emissions from sensor data (this study). **b)** Relationship between median day and night CO_2 emissions (g C m^{-2} d^{-1}) for all study sites and days. The black 1:1 line indicates that 75.2 % of observations exhibit enhanced nocturnal emissions. The inset illustrates the distribution of observations in the densest region of the graph.

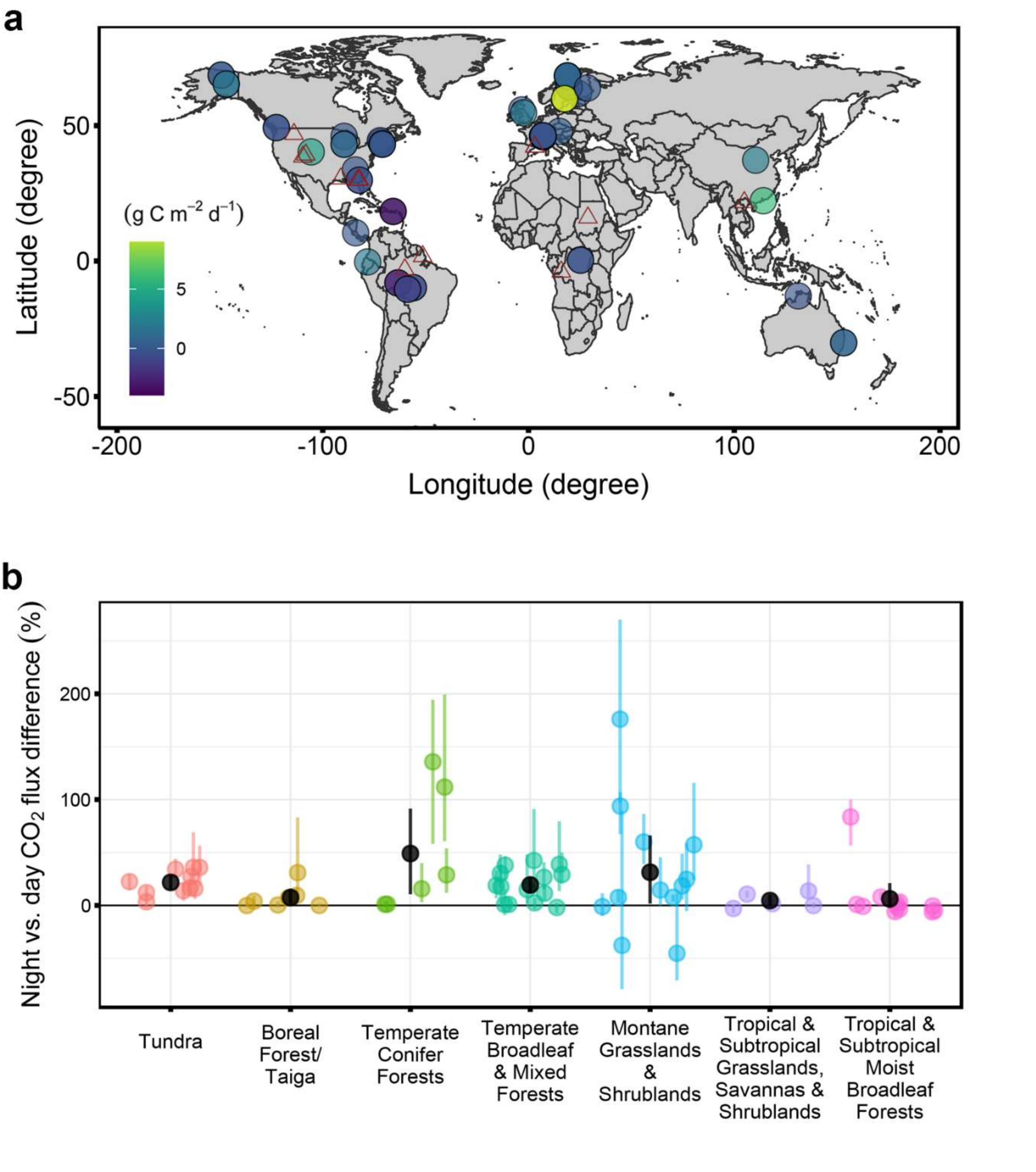

Figure 2. Geographical distribution of diel variation in stream CO_2 emissions. a) Global patterns of night-day differences in CO_2 emission fluxes averaged by stream (in g C m^{-2} $d^{-}1$; see Table S3 for a detailed summary). Triangles represent locations of studied rivers in Figure 4. **b)** Night-day differences in CO_2 emission fluxes averaged by stream, grouped by biome and sorted by descending latitudes (in %; see Table S3 for a more detailed summary). Biome assignment derived from Olson et al. (2001).

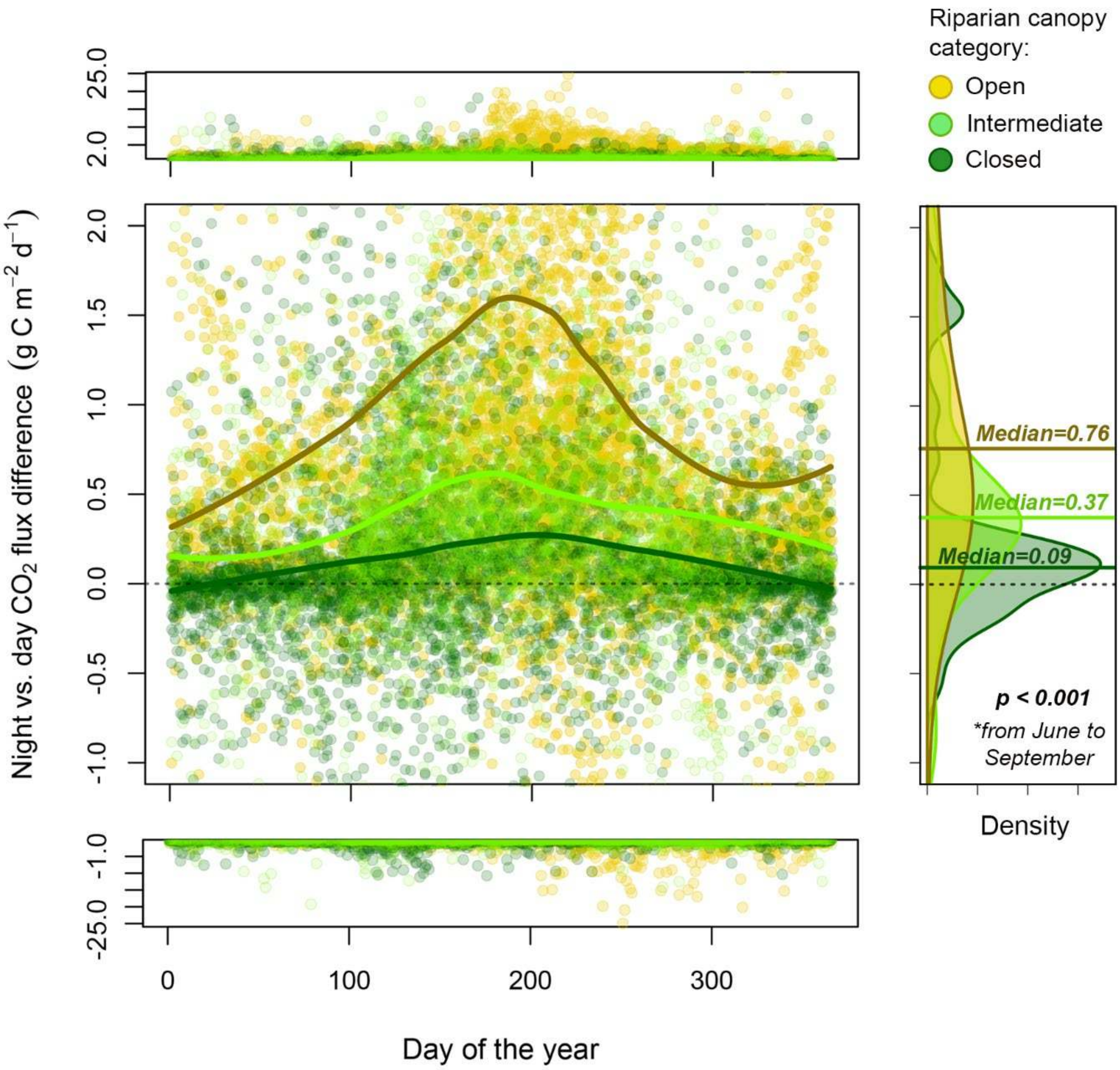

Figure 3. Seasonal pattern of diel changes in CO_2 emissions from streams. Seasonal variation in the night-day difference of CO_2 emissions (g C m^{-2} d^{-1}) grouped by riparian canopy cover category (open = yellow, intermediate = light green and closed = dark green; 33, 16 and 17 sites and 5780, 3814 and 5130 daily observations, respectively; see Methods and Table S2). The colored solid lines are locally weighted regression (LOESS) model fits for a visual interpretation. Panels at top and bottom show extreme positive and negative values, respectively (note y-axis breaks and change in scaling). Density plots show distributions of night-day differences of CO_2 fluxes (g C m^{-2} d^{-1}) grouped by canopy cover during summer. Differences between canopy levels were evaluated using the non-parametric Kruskal–Wallis test.

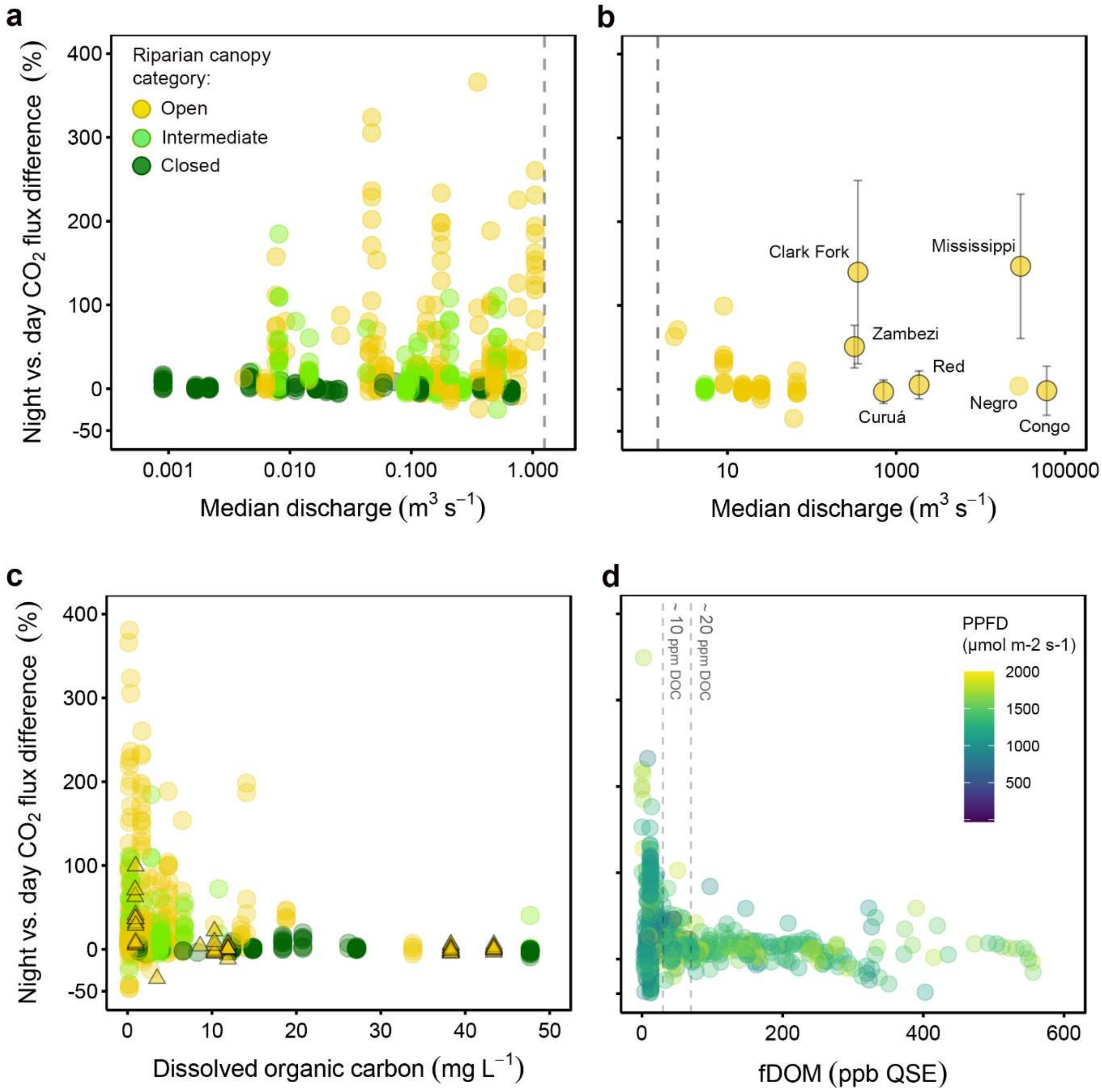

Figure 4. Night-day differences in CO_2 emissions along the river size and color continuum. Relationship between the night-day difference of CO_2 emission fluxes (%) and the median annual discharge ($m^3 s^{-1}$) for **a)** streams (median discharge below 1.5 $m^3 s^{-1}$, Figure S5) colored by canopy cover category, and **b)** rivers (median discharge above 1.5 $m^3 s^{-1}$). Each point represents a monthly average for each site, except data from the six additional rivers (circles with grey error bars) obtained from the literature (Table SX). **c)** Relationship between the night-day difference of CO_2 emission fluxes (%) and the mean dissolved organic carbon concentration (DOC) for streams (circles) and rivers (triangles), colored by canopy cover category. **d)** Relationship between the daily night-day difference of CO_2 emission fluxes (%) and the daily fluorescent organic matter concentration (fDOM, ppb QSE) for the five rivers in Florida with high-frequency water color data (Table SX) , colored by mean daily photosynthetic photon flux density (PPFD; µmol $m^{-2} s^{-1}$).